Applied Thermal Engineering 269 (2025) 126138

Contents lists available at ScienceDirect

Applied Thermal Engineering

journal homepage: www.elsevier.com/locate/apthermeng

Research Paper

Assessing the effect of size variation in graphite and alginate matrices for thermochemical heat storage

Jack Reynolds, Nigel Koungampillil, Jonathon Elvins *, Eifion Jewell, Justin Searle, Nicola C Mumford, Cameron Pleydell-Pearce, Richard E Johnston

Swansea University, Bay Campus, Crymlyn Burrows, Swansea SA1 8EN, UK

ARTICLE INFO

Keywords:
Thermochemical heat storage
Charging and discharging performances
Graphite-aided composite
Kinetic performance evaluation
Material characterisation
Bead size effects

ABSTRACT

The charging and discharging performance of thermochemical heat storage (TCHS) materials within practical applications will be influenced by key material and reactor properties such as thermal conductivity, ease of airflow through the material bulk and moisture exchange kinetics. This study examines the impact of varying the bead size of Alginate-Graphite-$CaCl_2$ composites on the thermal and kinetic performance under static and dynamic conditions. Successful synthesis was achieved, with variations in composite composition ascribed to differential shrinkage factors during freezing. XCT studies highlighted improved packing with decreasing bead diameter although this significantly increases the differential pressure across the bed. Smaller diameters result in increased water sorption, which corresponds with higher peak temperatures and sustained temperature elevation during discharging analysis. Charging materials at temperatures between 90–150 °C has minimal effect on the ultimate charge profile. However, materials with large diameters display an improved charging efficiency advantage up to a charging level of 50 % but ultimately the smallest composites exhibit a slight efficiency improvement at 95 % charge.

1. Introduction

The urgency to transition to sustainable energy sources has never been greater, especially as the global reliance on fossil fuels continues to significantly contribute to greenhouse gas (GHG) emissions. In 2020, the UK's residential sector alone was responsible for 16 % of the country's total GHG emissions, primarily due to thermal energy usage in heating, domestic hot water use and cooking [1]. Despite positive efforts to 'go green' which includes the rapid rollout of renewable electricity generation, transition to electric vehicles, and greater electrical storage capacity, emissions in the residential sector have remained relatively stable between 2014 and 2020. This stagnation underscores the need for more effective solutions to reduce energy demand on buildings and minimise the current reliance on fossil fuels for thermal generation [2]. The UK's Climate Change Act mandates a significant reduction in these emissions, necessitating a shift towards renewable energy sources and improved insulation in both new builds and the current housing stock [3,4]. Globally a similar trend holds true, within the European Union the combined industrial and residential heating demand in 2020 was just 10 % below that of the 2005–2009 period [5], despite mild winters and the global pandemic. Across the EU, domestic heating accounted for 28 % of the final energy consumption with industry and transport splitting the balance. Whilst global heat energy consumption increased by 6 %, only 50 % of this increase was provided through low carbon sources, with the majority of this within the building sector attributed to heat pump installations [6]. Advanced thermal energy storage (TES) technologies are an enabling technology, capable of integrating into all housing types and coupling with multiple renewable energy sources providing potential to time shift energy generation and consumption on a diurnal and seasonal basis [78].

Solar thermal energy can meet a building's energy needs during the summer, often exceeding demand during this period. However, it fails to meet energy demands in the winter when heating is most required. With the development of more efficient homes and the ability to store heat seasonally, the residential sector can make rapid strides in reducing its emissions.

Among TES technologies, thermochemical heat storage (TCHS) stands out for this use case. TCHS stores energy through reversible chemical reactions, offering higher energy densities and little to no

* Corresponding author.
E-mail addresses: J.d.p.reynolds@swansea.ac.uk (J. Reynolds), 955810@Swansea.ac.uk (N. Koungampillil), Jonathon.Elvins@Swansea.ac.uk (J. Elvins), E.Jewell@Swansea.ac.uk (E. Jewell), J.R.Searle@Swansea.ac.uk (J. Searle), n.c.mumford@swansea.ac.uk (N.C. Mumford), r.johnston@swansea.ac.uk (R.E. Johnston).

https://doi.org/10.1016/j.applthermaleng.2025.126138
Received 25 November 2024; Received in revised form 28 February 2025; Accepted 3 March 2025
Available online 4 March 2025

Nomenclature

Cp	Specific Heat Capacity (kJ/kg.K)
ΔT	Temperature difference (K)
CCP	Cubic Close Packed
CSA	Cross-Sectional Area
DCA	Dynamic Charge Analysis
DRH	Deliquescence relative humidity
HCP	Hexagonal close-packed
RCP	Random close-packed

Greek Letters

λ	Thermal Conductivity (W/mK)
Q	Energy (kJ)
m	Mass of air (kg)

Abbreviations

RH	Relative Humidity
SCA	Static Charge Analysis
SIM	Salt in Matrix
SVS	Static Vapour Sorption
TCHS	Thermochemical Heat Storage
XCT	X-ray micro-computed tomography

thermal losses compared to alternative methods such as sensible or latent heat storage. TCHS has shown potential in residential applications, where it can facilitate seasonal heat storage, as well as in industrial settings, where it enables the transport of heat between different sites [9,10]. A key area of research within TCHS is the development of 'Salt in Matrices' (SIMs), which involves embedding thermochemically active salts within porous matrices to enhance reaction kinetics and improve material stability [11–14].

The choice of matrix material is critical to the performance of SIMs. Expanded graphite (EG) has emerged as a leading candidate due to its high thermal conductivity and large surface area, which significantly enhance the heat transfer properties of TCHS composites [15–18]. However, the effectiveness of EG can be limited by additional processing steps, such as tableting, which reduce porosity and adversely affect mass transfer [15]. Recent advancements have focused on incorporating polymeric binders and utilising freeze-drying and moulding techniques to maintain porosity and improve the mechanical strength of EG-based composites [19–22]. One method for enhancing the performance and stability of these composites is altering salt loading [23–26].

The authors have previously assessed the performance of EG composites with varying quantities of salt incorporated into the porous structures, highlighting the importance of balancing energy storage density with porosity [27]. While high salt loading improves energy storage density, it compromises internal porosity, which significantly affects reaction kinetics, material stability, and the ability to contain salt deliquescence. A composite synthesised with 60 % saturated $CaCl_2$ at standard conditions (0.447 g salt/g water) showed a good balance between salt loading (70.9 wt%) and porosity (70.6 %), exhibiting competitive reaction kinetics and the ability to contain deliquescent salt. During the discharging cycle $CaCl_2$ gains water of hydration, emitting heat via an exothermic reaction given by:

$$CaCl_2 + xH_2O \rightarrow CaCl_2{\cdot}xH_2O + Heat \quad (1)$$

Conversely, the endothermic charging cycle (dehydration) reaction is given by

$$CaCl_2{\cdot}xH_2O + Heat \rightarrow CaCl_2 + xH_2O \quad (2)$$

Another important factor that would influence performance is composite size, although there is limited literature on this subject. Yang et al states that the effect of the composite PSD needs to be given more attention to provide information for developing large-scale TCES systems [28]. Zou et al. examined two sizes of K_2CO_3-impregnated vermiculite (0.4–0.8 mm and 3–6 mm), but significant variation in particle size within each group is still present [29]. The larger particle group held a larger proportion of salt while maintaining suitable porosity. Walsh et al. studied the effect of salt loading within vermiculite but did not assess composite size groups, instead using the full size distribution of the vermiculite available (1–6 mm) [26] Casey et al. also utilised matrices with a range of particle sizes (vermiculite 2–8 mm, zeolite 2–5 mm, silica gel 2–5 mm, and activated carbon 3 mm), but only sieved the matrices to narrow the size distribution to 3–5 mm [12]. Within these groups of varying particle size, the random packing arrangement will be more efficient as smaller particles can fill voids more effectively between larger particles [30]. However, this maximised packing isn't necessarily optimal for reactor performance, as it could increase the likelihood of condensation issues within a flow of humid air, as observed with vermiculite [14]. A consensus on reactor design for TCHS applications is yet to be established within the research community with configurations varying depending on the target process (open or closed systems) and materials used. Fumey et al review [31] multiple scaled reactor configurations providing insight into the best performances to date, and directions for further investigation. The reactor design challenge is to create an even air flow through a semi porous (at mm and μm scale) such that the salt is uniformly hydrated to its maximum hydrated state without excess hydration. Simulations offer a route to design optimisation, requires consideration of the complex momentum, energy and mass transfer processes. Models are able to predict reaction fronts and temperature profiles within a porous material salt hydrate / scaffold structure [32–34] Building on this approach, further studies could demonstrate annular reactor, outward flow was considered to provide an advantage over an inward flow [35]. Fundamental to any modelling success is the provision of material properties, porosity, thermal conductivity, real salt loading, salt distribution, particle size etc and high quality experimental data upon which a model can be validated. This is particularly important as new materials and material forms are developed.

For the current studies a simple cylindrical reactor is utilised within an open configuration with axial flow from base to top. This configuration has been shown to provide good thermal performance [32,35] however recent studies [35] have shown numerically that configuration changes could potentially improve exergy efficiency and reduce the pressure drop across the material bed.

Previous studies have highlighted the potential for EG/Alginate/$CaCl_2$ composites as thermal storage and heat delivery materials. The effect of particle size has not been reported in relation to the impact of the thermal and kinetic performance of the SIMs. Further to this the composite bead size will potentially influence salt loading, bead structure and packing factor – each effecting overall energy density. Sticking to a range commonly utilised for matrices within the application (3–7.5 mm), four composites of specific particle size (3, 4.5, 6, and 7.5 mm) are assessed for their influence on key characteristics such as thermal conductivity, flow through a packed bed, and charging/discharging kinetics. By systematically exploring the relationship between bead size and these performance metrics, this work aims to provide deeper insights into the design and optimisation of high-performance TCHS materials for practical applications.

2. Materials and methods

2.1. Materials

Anhydrous calcium chloride was purchased from Fisher Scientific and the equivalent salt solutions were prepared at room temperature with a $CaCl_2$ mass ratio of 0.447. Alginic acid sodium salt was obtained from Fischer Scientific in powder form and TIMREX® C-Therm 012

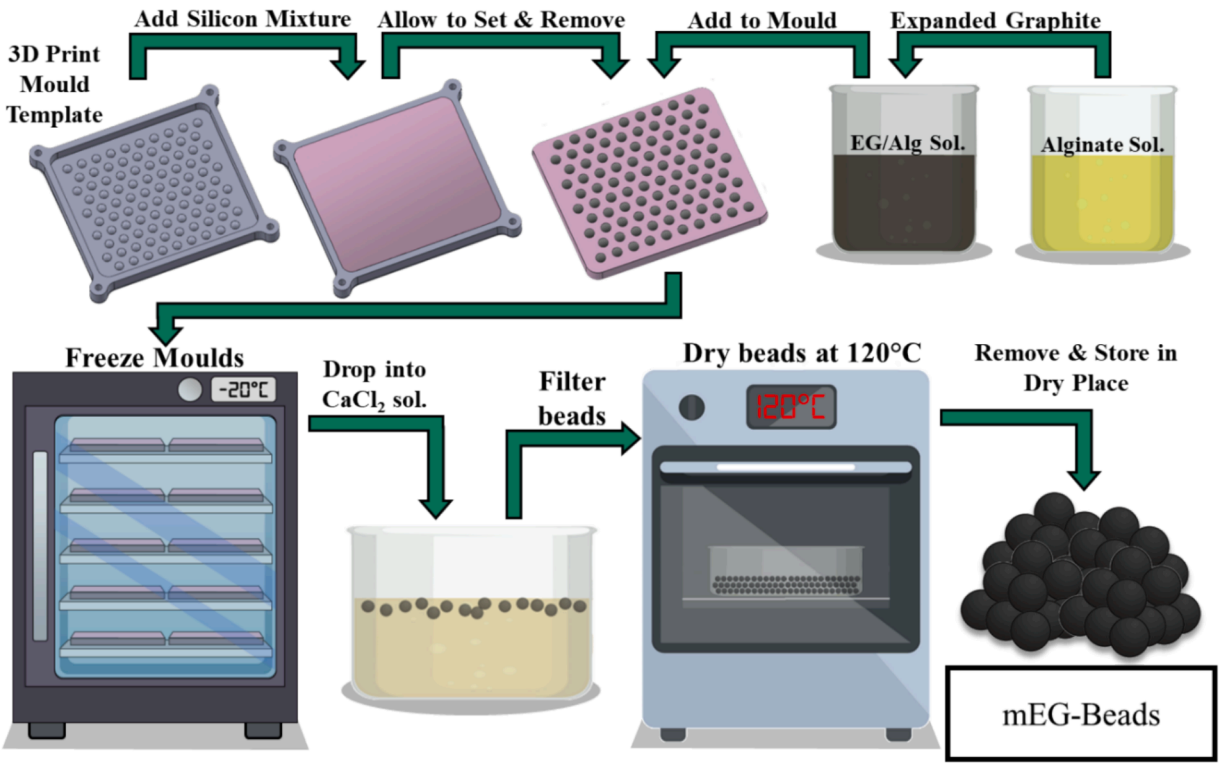

Fig. 1. Schematic illustration of size controlled synthesis of salt impregnated mEG/Alg beads using the mould method.

expanded graphite powder was purchased from Imerys Graphite & Carbon (Bironico, Switzerland).

2.2. Composite synthesis

Synthesis of the composite beads is shown schematically in Fig. 1, with the process fully described previously [27]. The moulds for bead formation are custom-fabricated in-house via a 3D-printed template that is utilised to create a flexible mould produced using Polycraft GP3481-F silicone rubber allowing for easy, but consistent alterations in bead size. Alginate solution is produced using a mixture of 1 g of alginate to 50 ml deionised water, stirred at 80 °C for > 4 h until fully dissolved. The graphite is added at a ratio of 6 g graphite per 1 g alginate solution and continuously mixed ensuring a homogenous blend. The resulting solution is transferred to the mould of desired bead size and frozen at −20 °C for > 2 h, allowing complete solidification of the beads to occur. The frozen beads are then transferred to the saturated calcium chloride solution for impregnation and cross-linking over a 24 h period. Once complete the beads undergo a filtration process and are dried at 120 °C before storage in an airtight container. For the current studies four bead sizes are evaluated with diameter sizes of 3 mm, 4.5 mm, 6 mm, and 7.5 mm. The 6 mm composite, the benchmark against previous studies [27], is labelled mEG-M−M, where the final'M' denotes a'medium' size. Consequently, the 3 mm composite is termed mEG-M−XS (Extra Small), the 4.5 mm as mEG-M−S (Small), and the 7.5 mm as mEG-M−L (Large). The prefix mEG denotes a milled expanded graphite is utilised within the composite.

2.3. Experimental procedures

2.3.1. Composite characterisation

The salt loading of the composites was determined using a titration analysis of chloride ion concentration, employing Mohr's Method. The method for this is a replication of the work conducted in the previous study [27].

The size distribution of the composites was examined using a Keyence VHX-7000 digital microscope. The bead diameter in the x and y planes was calculated for 20 beads from each sample, and an average value was determined.

The bulk density of the sample was calculated from their mass reading (measured on an Ohaus Scout STX223 with a readability of 0.001 g) in a known volume of a cylindrical container. The volume of the container is calculated from the filled mass of water (1 g = 1 cm^3).

The thermal conductivity of the synthesised composites was measured using a hot disk thermal constant analyser (TPS-1000, Hot Disk Inc., Sweden). Bulk samples were placed within a cylindrical container with an inner diameter of 60 mm and a height of 80 mm. A 4922 sensor with a radius of 14.6 mm was positioned at the centre of the cylinder, ensuring equal amounts of material (40 mm) above and below the sensor. Prior to measurement, the samples were dried at 120 °C for 24 h to achieve an anhydrous state. The thermal conductivity (k) and specific heat (C_p) of the bulk samples were measured four times for three filled containers of each material. This approach allowed for an average to be calculated, accounting for discrepancies resulting from variations in the packing of the beads during each measurement.

2.3.2. Flow characteristics

For the pressure testing, a simple fixed bed reactor was connected to a compressed air line, with the flow rate controlled by a Brooks MR3000 flow meter. The air was then passed through a fixed quantity of SIM as depicted in Fig. 2a. Differential pressure was recorded using tubes connected to a Testo 405, positioned both before and after the fixed bed. Four material depths and five flow rates were selected to develop a profile of the differential pressures. Additionally, a common mixed-size composite, consisting of expanded vermiculite and $CaCl_2$, was tested for comparison.

2.3.3. Static sorption and desorption analysis

Materials for Static Vapor Sorption (SVS) tests, are dried at 120 °C for 24 h to ensure the anhydrous state is achieved. A Memmert constant

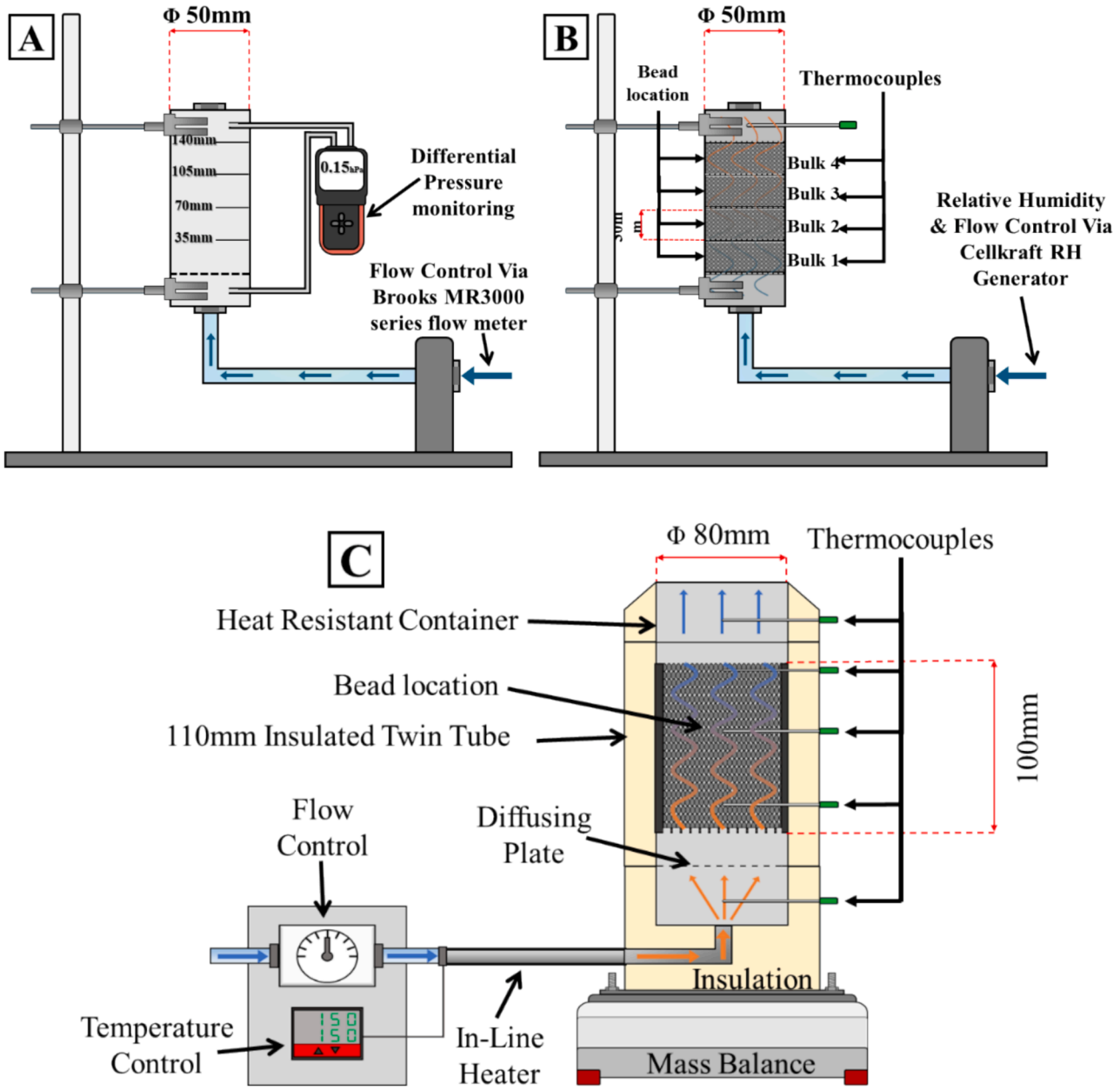

Fig. 2. (A) Experimental setup to monitor differential pressure through a packed bed system. (B) Modular design of a discharging reactor to analyse multiple sections of materials. (C) Experimental apparatus developed to assess the charging performance in an open-reactor.

climate chamber HPP110eco was employed to uniformly introduce moisture to 10 g of each material. A program was configured to maintain a constant RH (25 % and 50 %) and 25 °C for 24 h. Mass measurements were recorded in-situ throughout the 24-hour program.

For the reverse, static charging analysis (SCA) experiments were performed on 5 g of hydrated materials using the Ohaus MB120 equipment. The conditions selected were 90 °C, 120 °C, and 150 °C. The hydrated samples were synthesised to a hexahydrate state before conducting the experiment at conditions of 25 °C and 25 %RH until a mass increase corresponding to the hexahydrate was achieved.

2.3.4. *Dynamic charging and discharging analysis*

For discharging analysis a custom-built open reactor was designed to similar dimensions to the pressure testing. As a key interest was to observe the moisture absorbed throughout the packed bed, the reactor was designed to be separated into four modules, each of which could be tested for their moisture content within the MB120 moisture analyser. For the reaction, a continuous flow of humid air is directed upward through the fixed bed of materials from the base. A Cellkraft P-50 modular humidity generator is used to produce moist air which is fed into a reactor containing a predetermined volume of material (Fig. 2b). A thermocouple placed just above the final module is used to measure the temperature uplift across the reactor.

An open reactor design was employed for the dynamic charging analysis (DCA). A Leister Le Mini (In-line air heater) was used in combination with a Brooks MR3000 series flow meter, to create a flow of high-temperature air that passes through a packed bed of each material, with a volume of 400 cm^3 (Fig. 2c). The experiment was monitored using an Ohaus EX10202 scale to measure in-situ mass changes. Additionally, Type K thermocouples were strategically positioned at the inlet, bulk, and outlet locations to measure localised temperature variations. Three charging temperatures (90 °C, 120 °C, 150 °C), consistent with the SCA, and a flow rate of 50 l/min were selected for the analysis. Before conducting the experiment, as with the SCA, the material was hydrated at

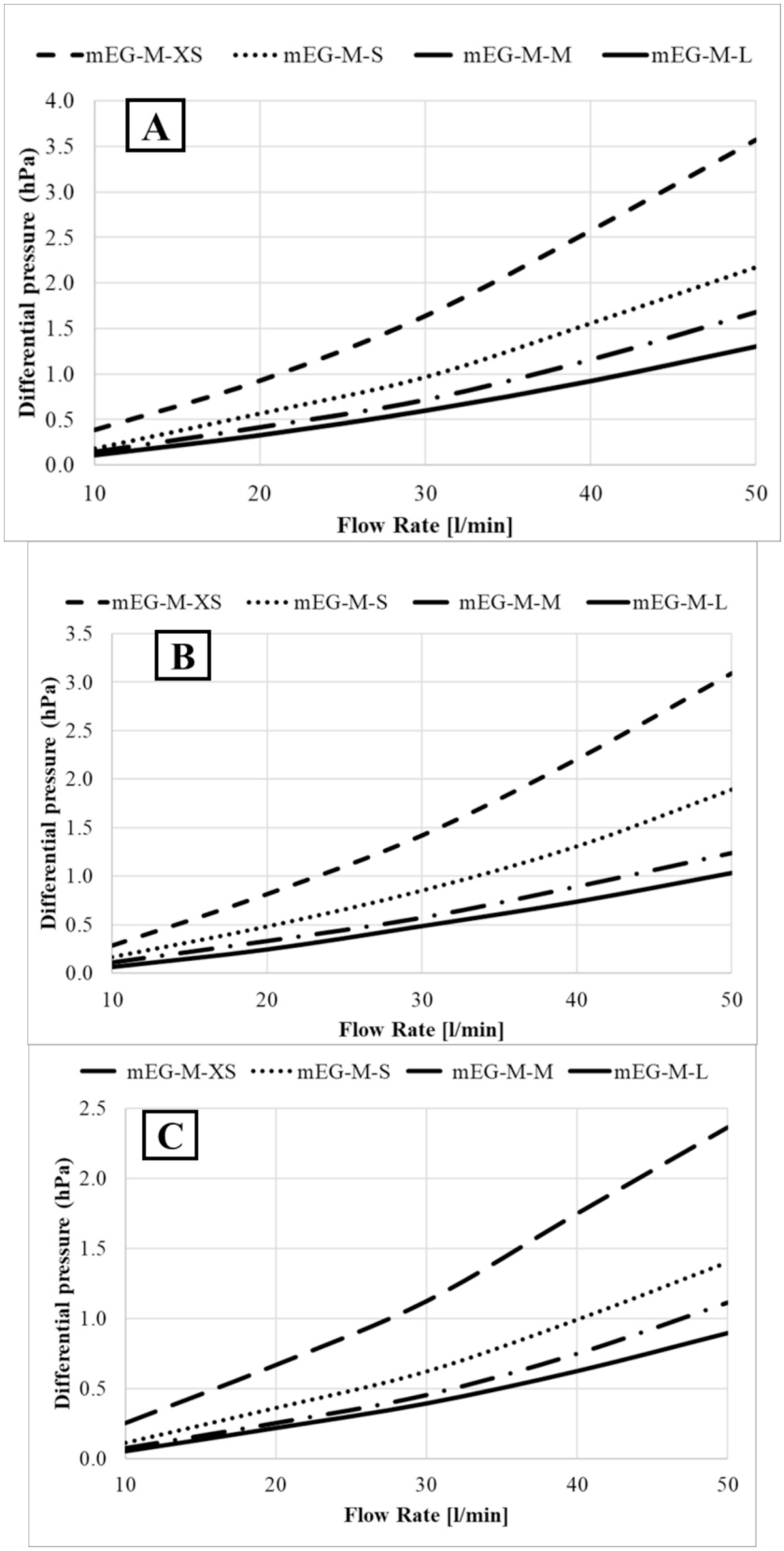

Fig. 3. Differential pressure across fixed bed reactor at a bed depth of 35 mm (A), 70 mm (B), 105 mm (C), and 140 mm (D).

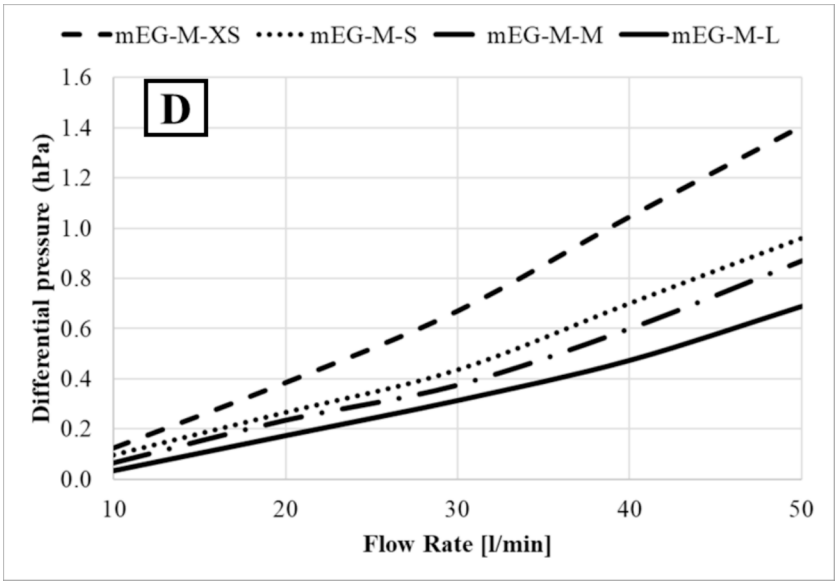

Fig. 3. (*continued*).

25 °C and 25 %RH until a mass increase corresponding to the hexahydrate was achieved.

2.3.5. X-ray micro-computed tomography

X-ray micro-computed tomography (XCT) was used to obtain 3D geometric data of graphite bead distribution and volume. Sealed containers were 3D printed for each set of beads to prevent dehydration of the beads caused by heat generated from the XCT equipment. The beads were imaged using the Nikon XT H 225 (Nikon Metrology) 3D X-ray micro-computed tomography system in the Advanced Imaging of Materials (AIM) Facility in the Faculty of Science and Engineering, Swansea university, UK. Each container was CT-scanned with a 120 kV tube voltage, and a current of 100 μA. Resulting in 3016 images per scan and a voxel (3D pixel) size of 34.25 μm. The tomograms were reconstructed from 2D projections using a Nikon cone-beam reconstruction algorithm and proprietary software (CTPro version 5.4, Nikon Metrology), resulting in an average file size of 9.5 GB.

2.3.6. Visualisation and segmentation

Dragonfly ORS Version 2022.2 for [Windows] visualisation software was used to view the 2D slices, 3D volumetric data, and produce binarized 2D slices [36].

3. Results & discussion

3.1. Composite characterisation

Characterisation data of the composite variants is shown in table 1 providing a summary of salt loading, bead size and both thermal and physical material properties.

Analysis of salt wt% across different bead diameters reveals a general trend of decreasing salt wt% with increasing bead diameter, with the exception of the mEG-M−M sample. Referencing the previous study, the equivalent sample of mEG-M−M (labelled as mEG60) demonstrated a salt wt% value of 70.9 %, aligning with this observed trend [27]. The deviation of mEG-M−M from this pattern could be related to the sample's shrinkage factor calculated from the mean diameter. The increased salt retention within the smaller composite size is likely due to smaller pore size exhibiting greater capillary forces and retaining an increased level of solution during the synthesis process.

This would agree with the work conducted by Zou et al [37], whereby larger pores can hold a greater quantity of salt. This shrinkage phenomenon highlights the complexity of factors influencing salt uptake and distribution within the composite materials. A potential variable affecting the shrinkage factor is the temperature differential between the salt bath and the frozen composite which can originate from multiple factors:

- The preparation of the salt bath, particularly the addition of $CaCl_2$, is an exothermic reaction. Typically, the pre-cast material is introduced to the salt bath once it stabilises to a temperature near to ambient conditions.
- Variations in the freezer's occupation of different thermal mass may result in differing initial temperatures of the frozen beads.
- Upon immersion in the salt bath, the immediate rate of temperature drop would be influenced by the beads' surface area.

This initial temperature difference at the gelation stage could conceivably impact the shrinkage factor, offering a potential explanation for the observed discrepancies in salt wt% and, by extension, bulk density across the examined bead sizes.

The observed values of bulk density exhibit a discernible trend, with the smaller samples (mEG-M−XS and mEG-M−S) displaying higher bulk densities compared to the larger samples (mEG-M−M and mEG-M−L). In an infinite space, the bulk density for identical materials would be expected to remain constant. However, within a finite space, edge effects are occurring, diminishing packing efficiency near the vessel's perimeter. Larger beads are likely to create more significant voids near the walls due to their curvature, whereas smaller beads can occupy these spaces more effectively. This is later visually observed in Fig. 4 and Fig. 5 during XCT analysis. This phenomenon is consistent with the differences observed between the smaller and larger sample groups. What remains more challenging to account for is the difference within the groups themselves; mEG-M−S exhibits a higher bulk density than mEG-M−XS, and mEG-M−L has a higher bulk density than mEG-M−M. This variation can once again be attributed to the shrinkage factor. mEG-M−S undergoes greater shrinkage compared to mEGM-XS, leading to a reduced internal porosity, thereby increasing both material and bulk densities. Similarly, mEG-M−L, experiencing greater shrinkage than mEG-M−M, follows the same pattern.

The data indicates a correlation where the thermal conductivity increases with the diameter of the composites within a packed bed. Although smaller beads, being more numerous, potentially create a higher number of contact points within the bed volume, the

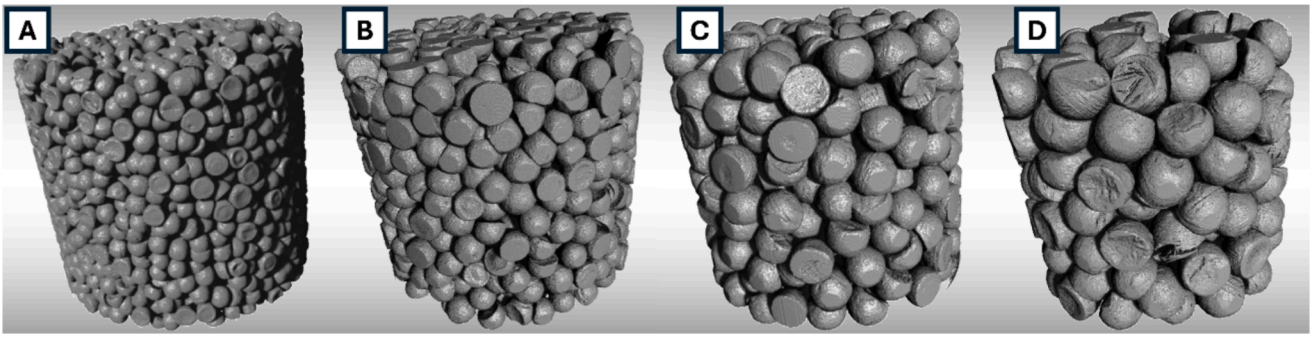

Fig. 4. 3D images produced from x-ray micro-computed tomography scan of reactor containing mEG-M−XS (A), mEG-M−S (B), mEG-M−M (C), and mEG-M−L (D).

effectiveness of these contacts for heat transfer may be compromised by their packing arrangement. Conversely, larger beads are likely to establish more substantial contact points with adjacent beads, facilitating enhanced pathways for thermal conduction.

3.2. Pressure analysis

In a comparative assessment of differential pressure, an experimental setup was employed in a tube reactor where compressed air was passed through a fixed bed at varying depths and flow rates.

As depicted in Fig. 3, the differential pressure curves in relation to flow rate for each material at specific material depths exhibit consistent trends; differential pressure increases exponentially with flow rate and rises with material depth under the tested conditions. Comparatively, mEG-M−M and mEG-M−L composites show closely aligned results at lower flow rates, which begin to diverge as the flow rate escalates. However, mEG-M−XS experiences almost double the differential pressure compared to mEG-M−S across most conditions tested. The formation of a condensation layer at the base of the fixed bed reactor is a known issue with TCHS composites, likely exacerbated by the deliquescence of $CaCl_2$ and the significant differential pressure. This observation suggests potential condensation issues for the 4.5 mm beads and almost a certainty for the 3 mm beads. Therefore, if higher flow rates are necessitated, larger bead diameters might be preferred to mitigate such issues. Conversely, lower discharge flows could permit the use of smaller diameters without concern for flow-related problems.

3.3. Fixed-bed XCT

To gain insights into the flow characteristics of bead composites of varying sizes within a fixed bed, X-ray micro-computed tomography (XCT) was employed as a non-destructive method for bulk analysis. XCT has previously been effectively used to monitor changes in composite size over 10 hydration/dehydration cycles in millimetre-sized composites for thermochemical heat storage applications [38]. Fig. 4 presents 3D models of the fixed bed reactors generated from the XCT scans. Qualitative analysis indicates that smaller diameter composites exhibit better packing, which is likely due to less efficient packing at the vessel wall boundary with larger beads.

The 3D models shown are composed of 1500 2D slices, which have been binarised, producing the black and white images depicted in Fig. 5b-e. In these images, the white areas represent voids where airflow can pass through the packed bed. Although only a single image is highlighted for each composite size, these effectively demonstrate the boundary effects and illustrate how packing efficiency decreases as composite size increases. By knowing the CSA of the reactor (ID = 50 mm, CSA = 1963.5 mm^2) and its equivalent diameter in pixels (1444 pixels), the pixel area is calculated to be 0.0012 mm^2. A Python script was utilised to count the white pixels in each of the 1500 reactor images, enabling the calculation of the void CSA distribution. To maintain consistency across composite sizes, images numbered 200 to 1000 were used in the distribution calculation, avoiding any inconsistencies in packing between the base and top of the reactor. The resulting void CSA distribution, presented in Fig. 5A, is expressed in terms of the count of images with CSA values falling within 0.25 % increment ranges. This

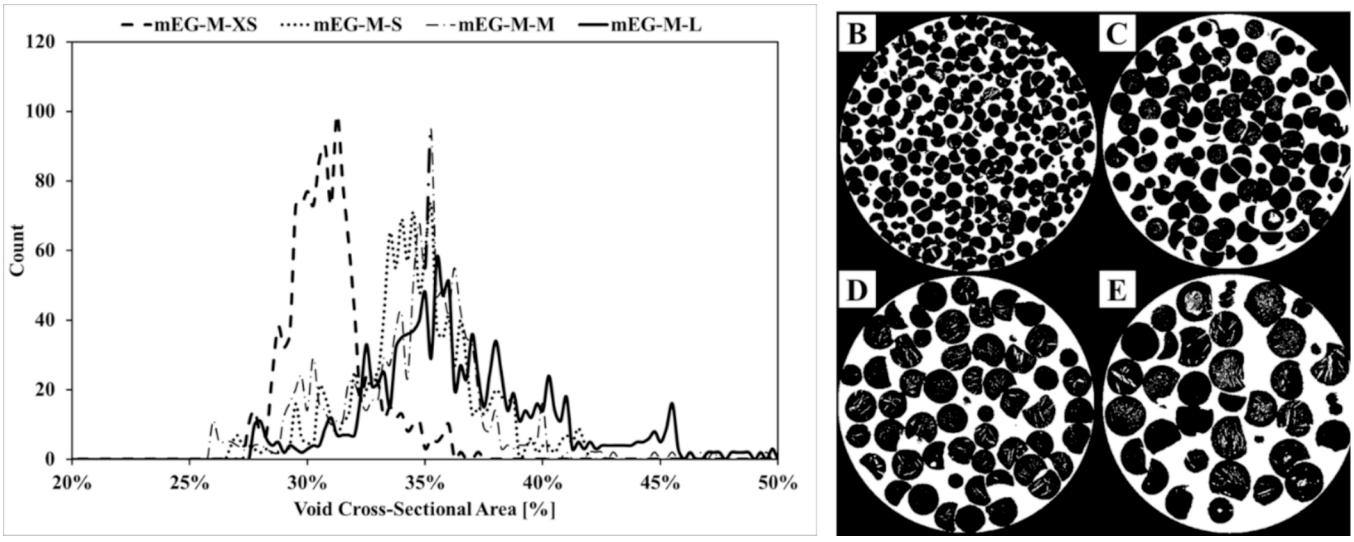

Fig. 5. (A) Void cross-sectional area (white area) as percentage of total reactor CSA and corresponding count for 1500 images taken during x-ray micro-computed tomography scans. Example binarized images used in calculation for mEG-M−XS (B), mEG-M−S (C), mEG-M−M (D), and mEG-M−L (E).

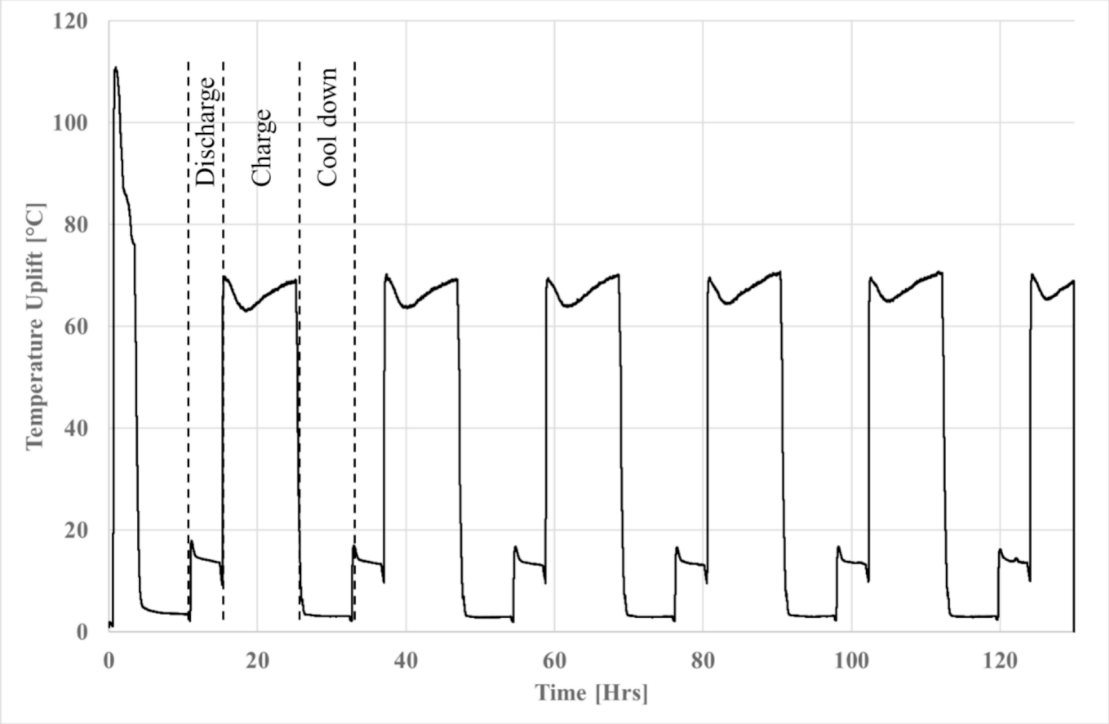

Fig. 6. Cyclic performance of the mEG-M−M variant.

approach allows for a detailed comparison of void space distribution across the different composite sizes.

The void CSA distribution curves exhibit a pattern that is inversely related to the differential pressure across the packed bed, as shown in Fig. 3. Specifically, the mEG-M−XS sample demonstrates a significantly lower CSA compared to the other samples. Additionally, the increase in CSA (evidenced by a shift to the right on the curve) becomes incrementally smaller as the composite diameter increases. This indicates that there is minimal reduction in packing efficiency when the diameter is increased from 4.5 mm to 7.5 mm. Table 2 presents the statistical data derived from these results. The mean and median void CSA values follow this trend; however, there is no noticeable difference in the mean CSA between the mEG-M−S and mEG-M−M samples, with only a slight difference observed in their corresponding median values. Despite this, Fig. 3 reveals a discernible difference in differential pressure between these two composite sizes, consistent with the overall trend. The standard deviation values indicate a wider range for the mEG-M−M sample compared to the mEG-M−S, which likely contributes to the observed lower differential pressure.

The packing efficiency is calculated from the percentage of each tomogram cross-sectional area that is not occupied by the mean void CSA, with each of the 3016 tomograms utilised to elucidate the 3D volume. As expected, the results show an increase in packing efficiency with decreasing composite diameter. These values all fall short of the ideal packing arrangements, such as cubic close-packed (CCP) and hexagonal close-packed (HCP), which both achieve a packing efficiency of 74 %. This discrepancy is primarily due to the random packing of spheres and the edge effects present in this fixed bed arrangement, along with synthesis Artefacts such as flat tops.

The packing efficiencies observed for the intermediate composites (mEG-M−S and mEG-M−M) align closely with the well-known value of random close packing (RCP), which is approximately 64 % [39]. Extensive studies, both experimental and computational, have shown that monodisperse spheres typically reach a maximum packing fraction of 64 % in random assemblies. The slightly higher values observed here (64.8 %) and the significantly higher efficiency for mEG-M−XS likely result from variations in composite size within the same sample group (making a polydisperse system), as well as slight deviations from a perfect spherical shape (such as the incorporation of a flat edge) which are artifacts from bead synthesis. Based on the differential pressure results, a packing efficiency of no more than 65 % should be targeted to enhance reaction performance and mitigate complications such as condensation.

3.4. Water sorption

The alteration in composite size prompts an examination of its impact on water sorption capabilities, with the fact that the contact area between particles and air is increasing as particle size decreases. To examine the influence of composite size on moisture adsorption, water sorption will be assessed under both static and dynamic conditions. Previous studies [19] have shown the potential for the mEG style alginate beads, highlighting the heat release capacity along with the consistency over multiple cycles. This is further verified in Fig. 6 below, showing six cycles over a 130 h period for the mEG-M−M variant. Each discharging cycle peaks between around 18 °C, with no degradation in performance observed.

3.4.1. Static Vapour sorption (SVS)

The impact of composite size on water sorption capacity was investigated using SVS tests, as depicted in Fig. 7. A quantity of 10 g of each sample variant was exposed to controlled conditions at 25 °C and RH levels of either 25 % or 50 % over a 24-hour period.

These specific conditions were chosen to contrast environments below and above the deliquescence relative humidity (DRH) of $CaCl_2$. The sorption curves can be characterised by their initial rapid uptake followed by a diminishing rate as the exposure approaches 24 h. Under the conditions of 25 %RH, which is below the DRH, the sorption curves of all four composites align closely up to a 20 wt% uptake. Beyond this point, the curves begin to diverge, displaying a trend in uptake rate that can be ordered as follows: S > XS > L > M. These marginal disparities are likely influenced by both the size of the composite and its salt wt%,

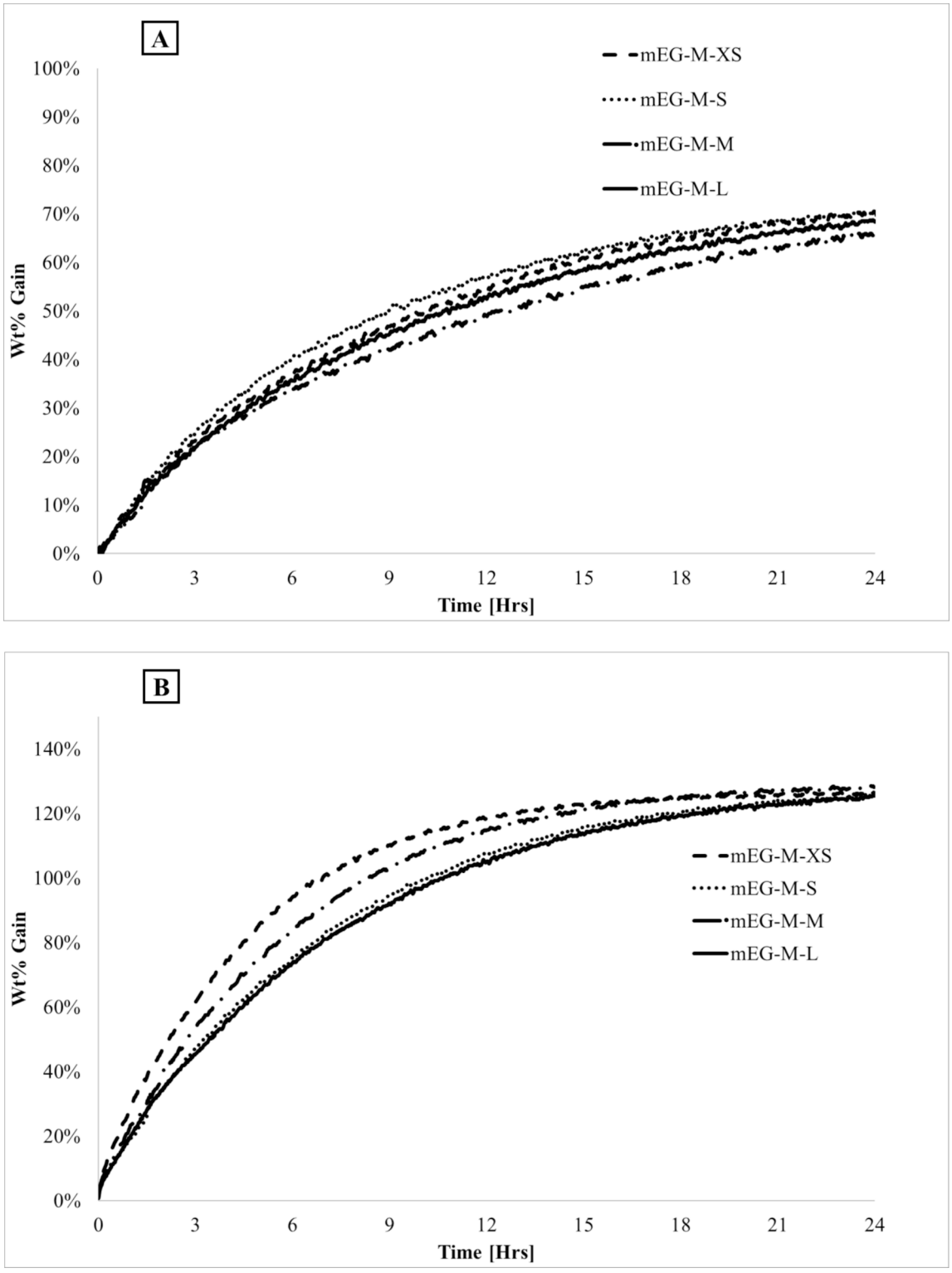

Fig. 7. SVS conducted on 10 g of anhydrous samples at 25 °C and 25 %RH (A) and 50 %RH (B).

with the latter appearing to exert a more significant influence. Notably, mEG-M−S exhibits a quicker sorption rate than mEG-M−XS, attributable to its lower salt wt%. A similar pattern is observed with mEG-M−L, which demonstrates a faster rate than mEG-M−M. At the condition of 50 %RH, which is above the DRH, the sorption curves of the three larger composites closely align up to a 20 wt% uptake, while the mEG-M−XS sample shows a noticeably higher rate from the outset. Beyond this point, the trend in uptake rate is as follows: XS > M > S > L. In scenarios where deliquescence occurs, the influence of composite size on the rate of uptake becomes more pronounced. However, there is an anomaly in this trend, as mEG-M−M exhibits a higher uptake rate than mEG-M−S. Considering the salt wt% values, this trend aligns with a higher uptake rate for increased salt content: 72.9 % > 72.9 % > 71.8 % > 70.3 %. Previous work [27] has shown that increasing the salt content results in increased filling of voids and more salt within the surface region. Hence for mEG-M−M and mEG-M−XS, the increased salt within this region

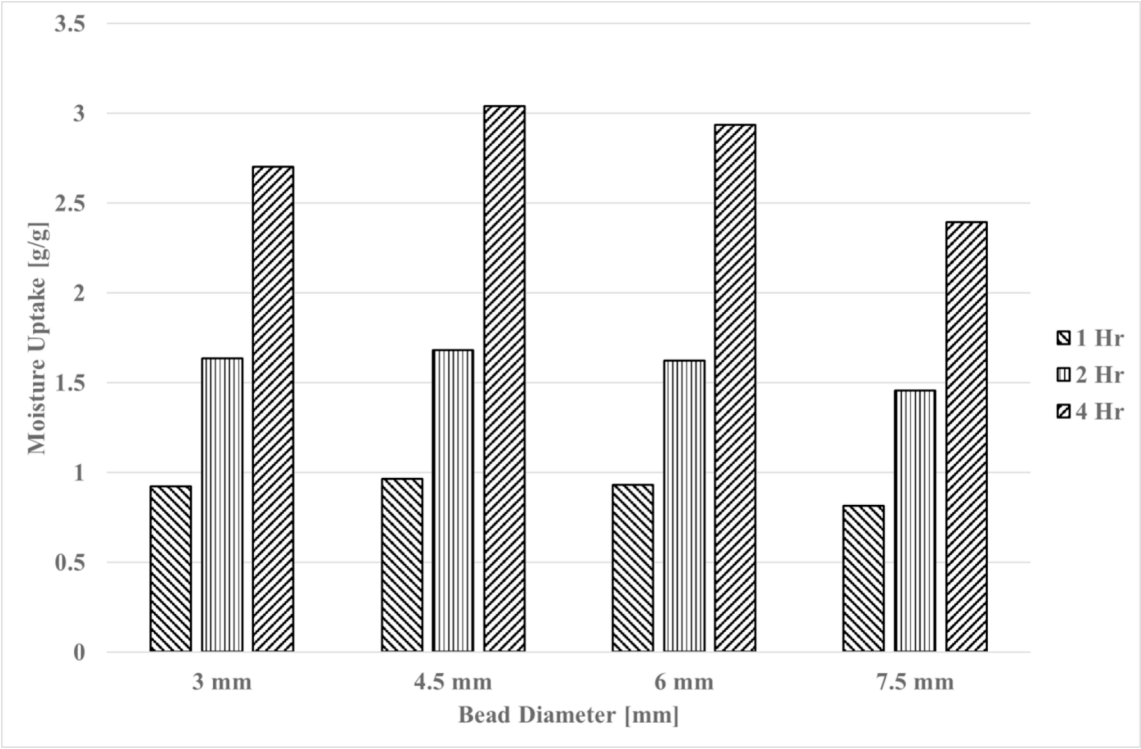

Fig. 8. Total moisture uptake for the four combined fixed-bed modules subjected to discharging reactions at 50 % RH and 25 °C with a flow rate of 30 l/min. Moisture uptake quantified using external moisture analyser at 1, 2, and 4 h post-reaction stage completion.

will lead to a higher uptake rate, when compared with the lower salt content composites. For the mEG-M−S sample, another influencing factor is likely the shrinkage factor; mEG-M−S experiences the greatest shrinkage, which would reduce internal porosity. However, this does not seem to counterbalance the effect of bead size, resulting in mEG-M−L exhibiting the slowest uptake rate.

3.4.2. *Dynamic sorption in a packed bed*

To evaluate the dynamic sorption characteristics within a packed bed environment, the modified discharge reactor, as detailed in Section 3.13, was employed. This reactor features a modular packed bed design, which facilitates the independent assessment of moisture uptake in each module, allowing for an understanding of how moisture is absorbed through the depth of the packed bed. For these dynamic sorption tests, a single set of conditions was chosen: 25 °C, 50 %RH, and a flow rate of 30 l/min. The experiments were conducted over three time intervals: 1 h, 2 h, and 4 h. The reactor is divided into four modules, each with identical volume, allowing for the calculation of four distinct moisture values after each reaction time. Each material was evaluated at all three time intervals, and an additional experiment was conducted using a mixture of all four materials, arranged in a graded fashion with the largest beads at the bottom and the smallest at the top of the reactor. This mixed-material setup was examined over the 4 h period only.

3.4.2.1. Total moisture uptake. Fig. 8 illustrates the cumulative moisture absorption across the four packed-bed modules for each composite size over the three time frames tested with uptake relative to the dry mass of the sample. There is a clear trend indicating increased moisture uptake with decreasing composite diameter. This could be attributed to the larger surface area available for moisture absorption in composites with smaller diameters, which allows more extensive contact with the reacting air. Moreover, the materials' hygroscopic nature means that a higher pressure would likely expedite absorption kinetics, thus enhancing moisture uptake.

Additionally, a higher differential pressure across the packed bed, as previously illustrated in Fig. 3, would increase the mass transfer rate of water molecules from the air to the internal porous structure of the composite material. For instance, at a bed depth of 140 mm under the conditions considered here, the differential pressure values for 3 mm, 4.5 mm, 6 mm, and 7.5 mm diameters are 1.64, 0.97, 0.72, and 0.62 hPa respectively, aligning with the observed trend. As anticipated, the mixed composite experiment yielded a total moisture uptake that falls between the two extremes observed for the mEG-M−XS and mEG-M−L samples. This outcome was predictable, considering the increased surface area available for sorption and the elevated pressure above the first module in the fixed bed, which would both contribute to higher mass uptake compared to a bed composed solely of mEG-M−L. However, the specific positioning of its performance, being just below the mEG-M−M sample, was less expected. This suggests that factors beyond mere surface area and initial bed pressure, possibly including the distribution of composite sizes and their individual sorption rates, play a role in the dynamic sorption process within a mixed particle size packed bed system.

3.4.2.2. Sectional moisture uptake. By examining the moisture content in each individual section over three time intervals, a dynamic profile of moisture distribution throughout the entire fixed bed is constructed, as depicted in Fig. 9. Across all samples and time points, the highest moisture uptake is consistently observed in the first section, progressively diminishing towards the fourth section. Notably, the difference in moisture uptake between sections, and how this spread changes over time, differs among the samples. This characteristic spread provides an indication of the uniformity of moisture absorption within the bed at different intervals.

During the initial hour of the dynamic sorption test, a marked difference in moisture uptake is evident in the first section of the reactor. The trend clearly demonstrates a higher moisture uptake for composites with smaller diameters. Specifically, the mEG-M−XS composite absorbs nearly twice the amount of moisture compared to the mEG-M−L within this section, underlining the accelerated absorption kinetics associated with decreased composite size. Within sections 2-4, the variation in

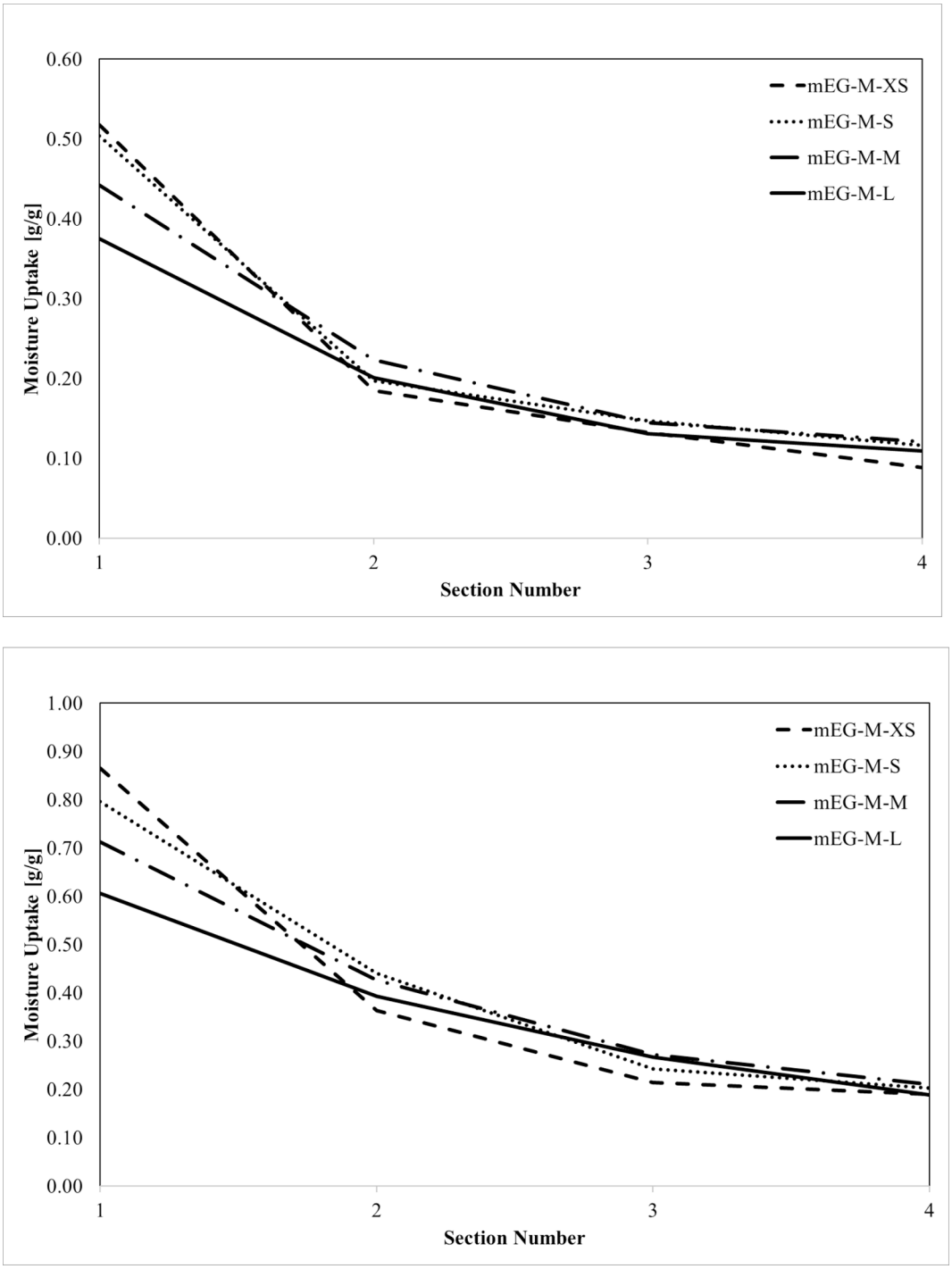

Fig. 9. Comparative moisture uptake across four fixed-bed module sections with varying particle sizes, measured at 1-hour, 2-hour, and 4-hour intervals.

moisture uptake becomes less pronounced but, despite this, the trend remains, with smaller composites exhibiting a marginally higher uptake, and thereby supporting the initial observations regarding composite size and moisture absorption.

After two hours of discharging under consistent conditions, the trends in moisture uptake within section 1 continue to be evident, however the difference between the mEG-M−XS and mEG-M−L composites has diminished, with the mEG-M−L now capturing approximately 2/3 of the moisture taken up by the mEG-M−XS sample. A notable shift is observed in the latter sections; for instance, in section 3, the order of moisture uptake is altered, with mEG-M−XS showing the least uptake and mEG-M−M the most. Although these differences are still minor at this stage of the experiment, they suggest that larger composite diameters may facilitate a more even distribution of moisture through the packed bed, whereas smaller composites might be impeding moisture movement beyond the initial sections.

The four-hour mark provides a more developed view of the moisture distribution across the fixed bed. Consistent with earlier observations, section 1 across all materials shows the highest moisture uptake, with the mEG-M−L now exhibiting moisture levels approximately 70 % of that of mEG-M−S. The differentiation in moisture uptake becomes more pronounced in the later sections of the bed. Notably, mEG-M−XS registers

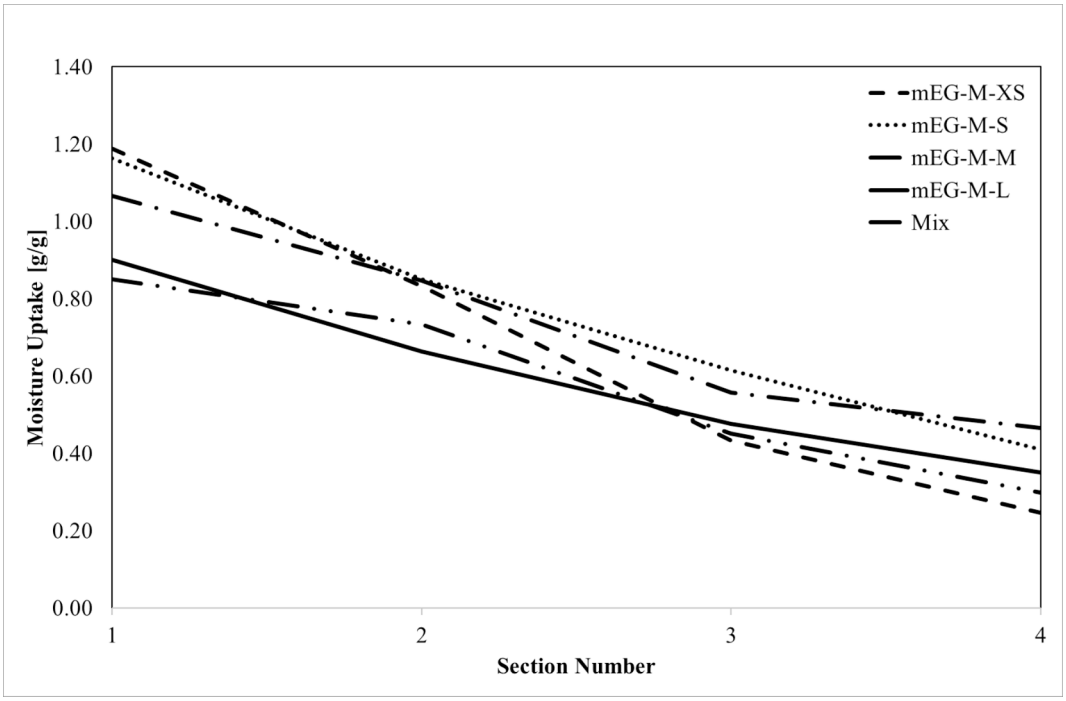

Fig. 9. (*continued*).

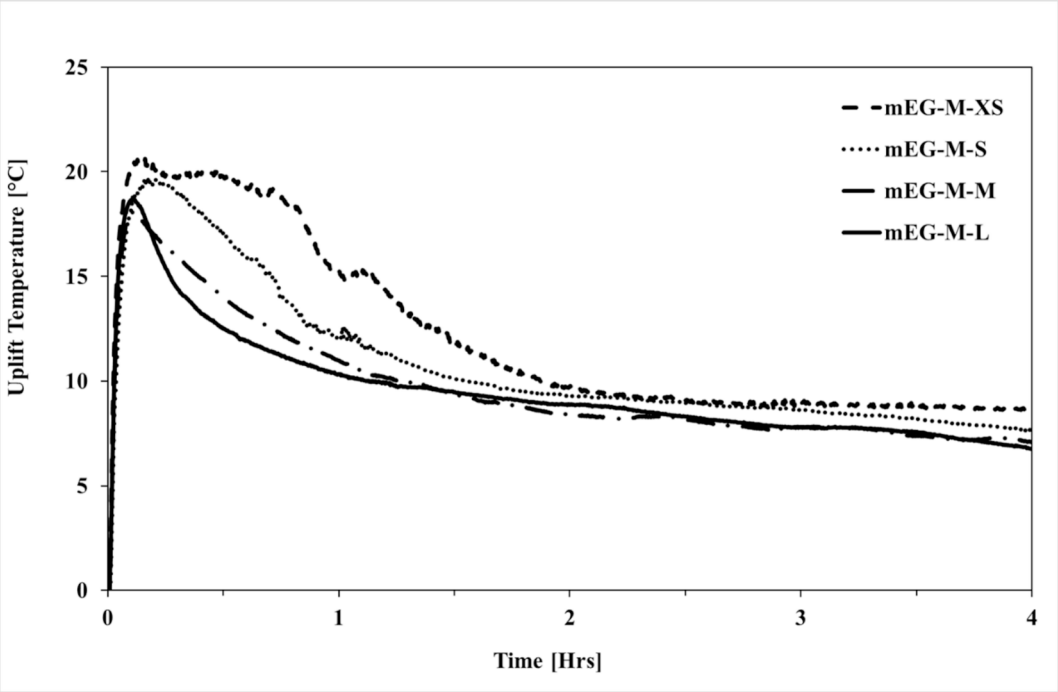

Fig. 10. Temperature uplift curves over a 4-hour discharging period within the four component modular discharging reactor, operating at 50 %RH and 25 °C with a flow rate of 30 l/min.

the lowest uptake at section 4, while mEG-M−M has the highest, followed by mEG-M−S. This suggests that the factors influencing uptake rates are multifaceted, with ease of airflow, as indicated by a smaller pressure drop, favouring the larger beads, and the increased surface area associated with smaller beads enhancing moisture absorption. The observed pattern seems to reflect a balance between these two factors.

When evaluating the uniformity of moisture distribution across the bed, or the difference between moisture uptake in section 4 versus section 1, the larger samples demonstrate a more balanced distribution. Specifically, mEG-M−M and mEG-M−L show moisture uptakes in section 4 that are 40.2 % and 38.2 %, respectively, of the values in section 1. In contrast, mEG-M−XS and mEG-M−S have proportional uptakes of 19.8 % and 32.3 %, respectively. This indicates that the larger composites achieve a more even distribution of moisture throughout the bed, which could be advantageous for certain applications requiring uniform moisture content.

Table 1
Composite Characterisation.

Sample	Salt Wt [%]	Bulk Density [g/cm^3]	Target Diameter [mm]	Mean Diameter [mm]	Shrinkage Factor [%]	Salt Volumetric Density [g/cm^3]	T Conductivity [W/mK]
mEG-M−XS	72.9	0.49	3.0	3.1	88.8	0.36	0.30
mEG-M−S	71.8	0.51	4.5	4.5	85.7	0.37	0.32
mEG-M−M	72.9	0.41	6.0	6.4	91.1	0.30	0.33
mEG-M−L	70.3	0.44	7.5	7.9	89.7	0.31	0.36

In the mixed sample experiment, whereby section 1 comprises the largest beads through to section 4 that contains the smallest, the moisture uptake profile observed across the four sections after four hours presents improved characteristics. As anticipated, the moisture uptake in section 1 closely aligns with that of section 1 from the mEG-M−L experiment, given the identical material composition in this initial section. However, moving beyond the first section, each subsequent section in the mixed sample demonstrates an increased uptake compared to its corresponding pure sample counterpart. This is most pronounced in section 4, where the moisture uptake surpasses that of the pure mEG-M−XS section 4 by 40 %. Not only does the mixed sample show an elevated moisture uptake in the latter sections, but it also exhibits the most evenly distributed moisture uptake throughout the bed, with section 4 achieving 40.3 % of the moisture uptake recorded in section 1.

3.5. Discharging analysis

The dynamic sorption tests, which also included temperature measurements, provide insights into the uplift temperature behaviour across the fixed-bed reactor. Fig. 10 presents the temperature profile of airflow through the reactor for the four materials and the mixed material experiment over a 4 h period. Several key observations can be made:

Peak Temperature Time: There is a noticeable trend where the time to reach peak temperature increases with decreasing particle diameter. The mEG-M−XS sample displays some variability, which somewhat disrupts this pattern. However, the reason for this observed trend is that each material heats at a similar initial rate, and the later peaks are primarily due to achieving higher uplift temperatures taking a longer time.

The energy evolved during the discharge cycle is calculated using equation (3):

$$E_{EV} = mC_p\Delta T_{Ave} \tag{3}$$

Where:

Q = Energy (kJ).
m = Mass of air (kg).
C_p = Specific Heat Capacity kJ/ kg.K.
ΔT = Temperature difference (K).

The error attributed to the energy calculations is given by:

$$u_{E_{EV}} = \sqrt{\left(\frac{\partial E_{EV}}{\partial m}u_m\right)^2 + \left(\frac{\partial E_{EV}}{\partial C_p}u_{C_p}\right)^2 + \left(\frac{\partial E_{EV}}{\partial \Delta T_{Ave}}u_{\Delta T_{Ave}}\right)^2} \tag{4}$$

where u_m, u_{Cp}, $u_{\Delta TAve}$ are the errors related to the individual factors for the energy evolved. The maximum absolute error for ΔT is 1.3 °C, with an absolute expanded uncertainty with coverage factor of 2 being 2.6 °C. Maximum relative error for the energy evolved is 0.36 % and the absolute expanded uncertainty with coverage factor of 2 is 0.27 kJ.

Maximum Temperature at Peak: The smaller the particle size, the higher the initial peak temperature, which can be attributed to the greater surface area facilitating a faster reaction rate. The increase in surface area will also increase the heat transfer from material to air flow. Despite larger particles having better thermal conductivity in a static bed, as indicated in Table 1, the increased surface area becomes a dominant factor for heat transfer during airflow.

Table 2
Void CSA statistical data.

Sample	Mean Void CSA [%]	Median Void CSA [%]	Std. Dev [%]	Packing [%]
mEG-M−XS	31.6 %	30.9 %	3.6 %	68.4 %
mEG-M−S	35.2 %	34.7 %	4.0 %	64.8 %
mEG-M−M	35.2 %	35.0 %	5.0 %	64.8 %
mEG-M−L	37.2 %	36.0 %	5.2 %	62.8 %

Table 3
Summary of energy evolution during 4 h discharging cycle.

Sample	Total energy evolved (kJ)	Peak energy evolved (kJ)	Time to peak energy (minutes)
mEG-M−XS	153.2	0.017	10.3
mEG-M−S	141.2	0.015	13.1
mEG-M−M	125.1	0.013	7.4
mEG-M−L	119.5	0.014	9.4

Peak Temperature Width: The width of the temperature peak generally broadens with smaller particle sizes. The mEG-M−XS shows more variation, yet the trend still stands. This expansion could be due to the greater surface area allowing for more immediate salt reaction without being limited by mass transfer through the hydrated layers on the bead surfaces. The degree of mass transfer through hydrated layers required to reach unreacted salt increases with increasing bead size.

Temperature Uplift after 4 Hours: Smaller particles maintain a higher temperature uplift after 4 h, likely due to their smaller size which minimizes mass transfer resistance, allowing for sustained reaction kinetics as moisture uptake progresses through the fixed-bed.

Energy evolved during the discharging period: Table 3 provides a summary of the energy evolved, peak energy and time to peak energy during the 4 hr discharging period.

From these data it can be seen that the total energy evolved in mEG-M−XS is maximum followed by each sample in increasing size. The smaller bead size affords more ready access to salt at the centre of the bead promoting rapid release of energy, allowing for greater energy release prior to any limiting effects that may occur. The smaller bead size also has enhanced packing allowing for improved thermal transfer into the passing air stream.

When correlating these observations with the total moisture uptake data (Fig. 8), it is evident that the mEG-M−XS has the highest moisture absorption after 4 h, suggesting a more extensive degree of discharging conversion and higher heat output. As well as this, the data in Fig. 9 indicates that section 4 of the fixed bed shows a notably lower moisture uptake compared to other sections, which despite an uneven moisture uptake distribution, there remains a significant amount of unreacted salt

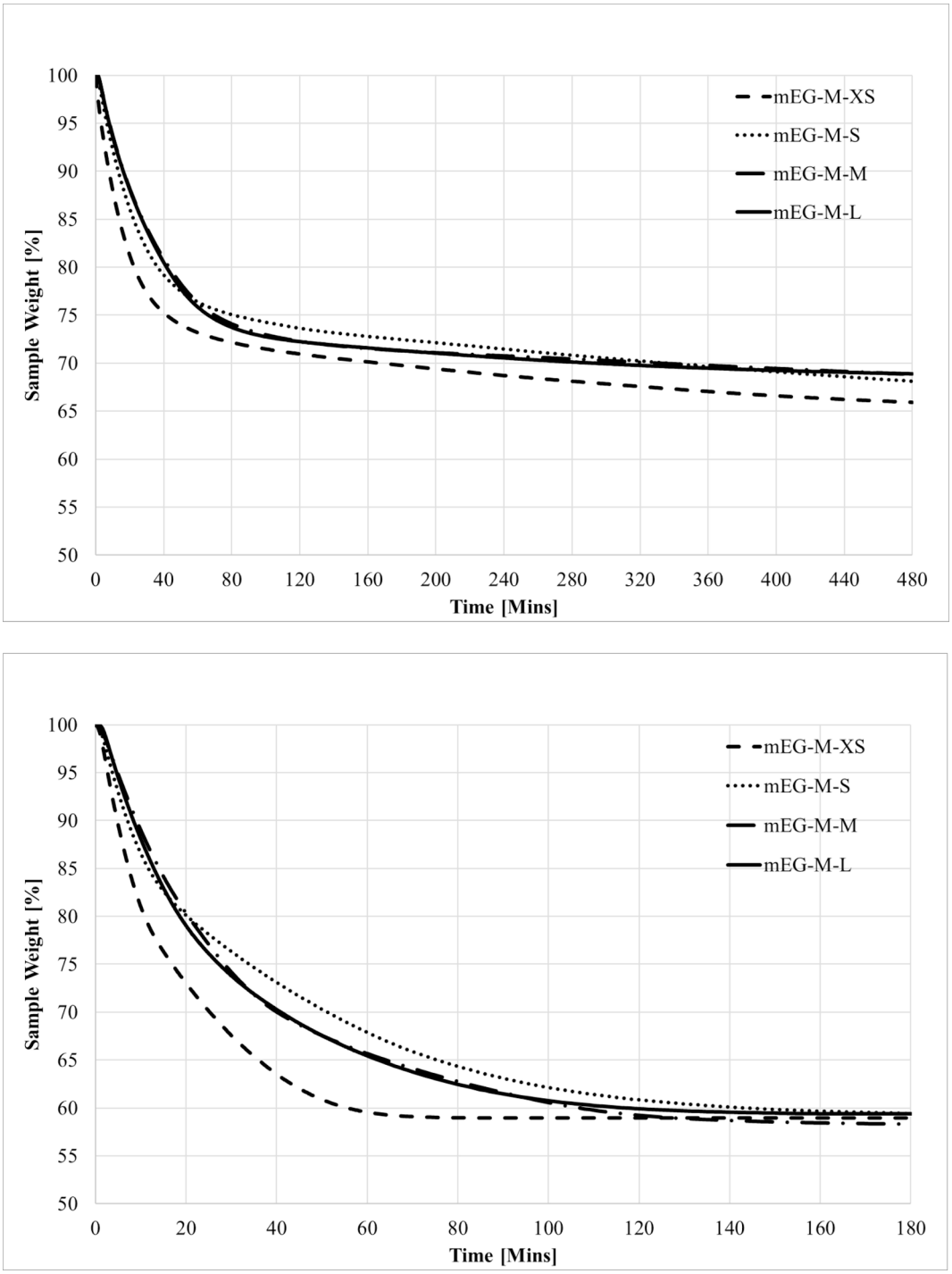

Fig. 11. SCA curves obtained from the MB120 moisture analyser at 90 °C (A), 120 °C (B) and 150 °C (C) for four materials hydrated to the hexahydrate hydration state.

in the upper sections. These sections are less hindered by the hydrated salt layers, allowing for more significant heat release at the longer discharging durations.

In examining the mixed sample experiment, this configuration achieves an intermediate peak temperature height and width compared to the four pure samples. Notably, after four hours of discharging, the temperature uplift for the mixed sample is higher than that of all other individual samples, indicating that this mixed configuration bed may offer the most optimal performance within the reactor. This superior temperature profile is accomplished even with the most uniform moisture distribution across the fixed bed and the lowest moisture uptake in section 1, as shown in Fig. 9. Such a profile is advantageous, as it reduces the risk of over-hydration at the base of the bed, a particular concern of the mEG-M−XS sample. Furthermore, the total moisture uptake, as depicted in Fig. 8, is comparatively low, implying that the mixed sample not only ensures more efficient discharging reactions but also retains a greater potential for energy release after 4 h.

The practicalities of operational use for such materials have been reported previously [27] whereby the use of TCHS materials as primary heating requires careful consideration of the reactor design and

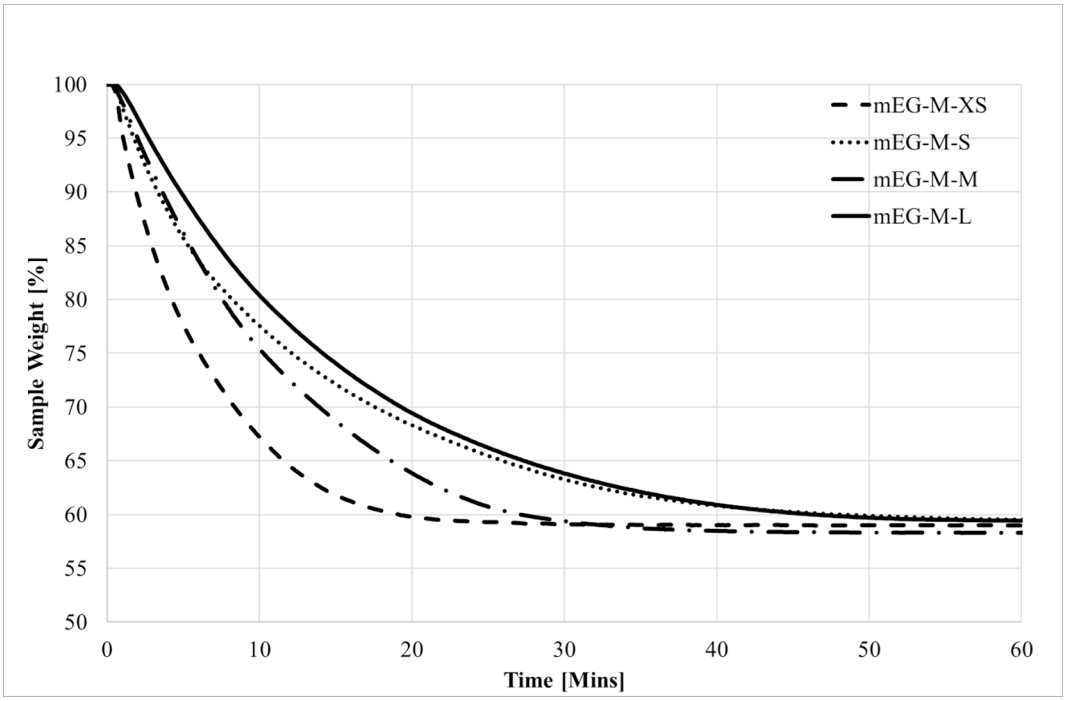

Fig. 11. (*continued*).

operational strategy, with either dynamic heating for short periods or a continuous lower level 'background' heating preferred. Alternative applications include integration with air source heat pumps, providing an initial temperature evaluation on the ambient inlet air resulting in reduced demand on the heat pump and an increased coefficient of performance.

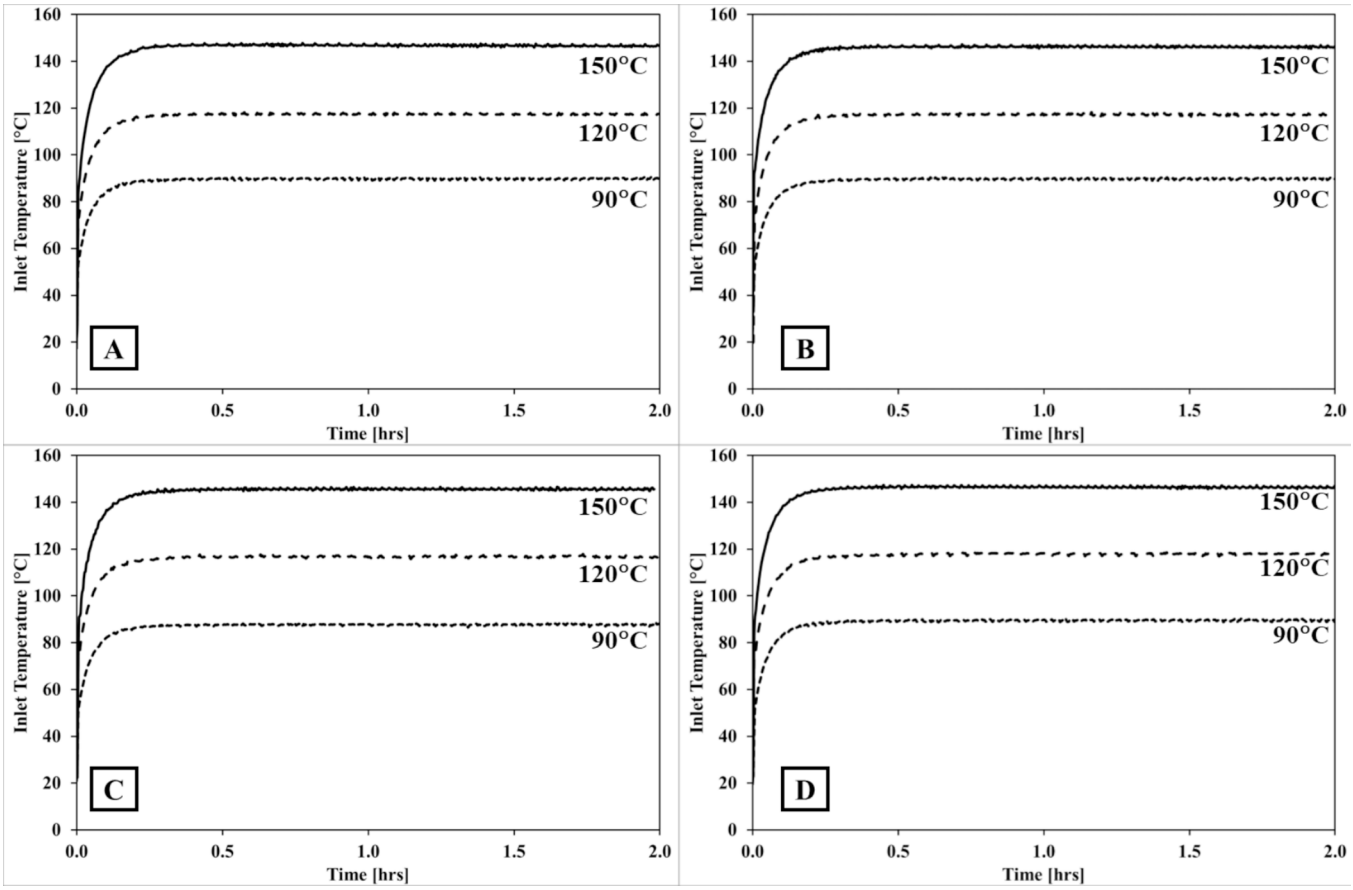

Fig. 12. Inlet Temperature profiles in Open Charge Reactor for mEG-M−XS (A), mEG-M−S (B), mEG-M−M (C) and mEG-M−L (D).

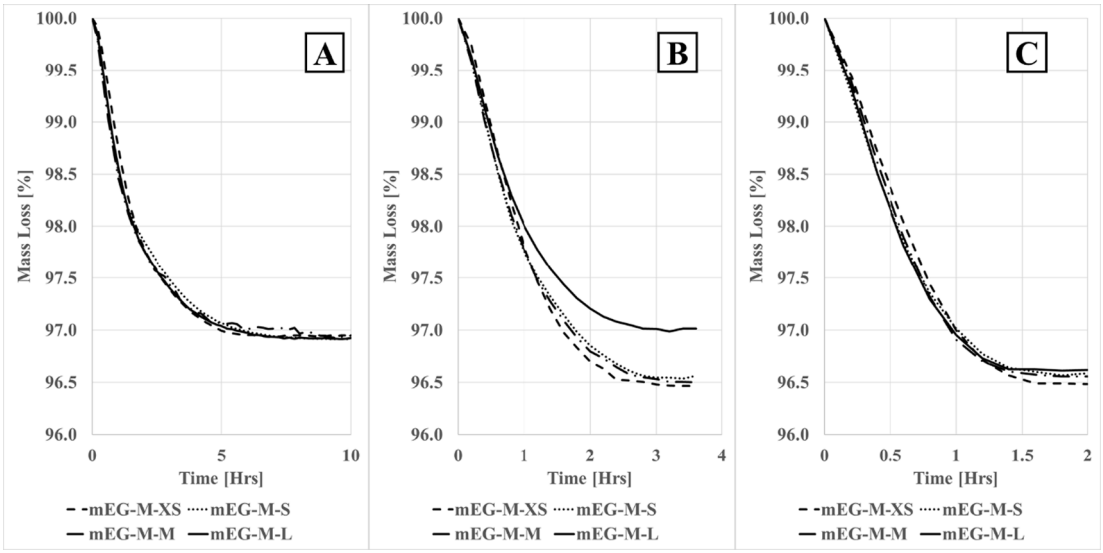

Fig. 13. Mass (A-C) and Outlet temperatures (D-F) curves with respect to time for DCA of the four composite materials at flow rates of 50 l/min and flow temperatures of 90 °C (A/D), 120 °C (B/E) and 150 °C (C/F).

3.6. Charging analysis

The charging performance of composites with varying particle sizes is assessed through both static and dynamic charging methods at two critical temperatures, 120 °C and 150 °C, with a focus on samples hydrated to their hexahydrate state. In addition to the final moisture content determined via the same static charging procedure as section 3.4.1, the static charging profiles will be examined and subjected to further analysis here.

3.6.1. SCA – Hexahydrate

Fig. 11 displays the SCA results for four composite samples in their hexahydrate state, subjected to static charging conditions of 90 °C, 120 °C, and 150 °C. The SCA uses 5 g of hexahydrate material, evenly hydrated as described in section 2.3.4, eliminating intra-sample variability created through the dynamic processes (e.g. variability from bottom to top of the individual sections).

In all temperature scenarios, the mEG-M−XS composite with the smallest bead diameter, exhibits superior charging rates compared to the larger-sized samples. This performance indicates that smaller bead diameters facilitate faster charging processes, likely due to the increased surface area. However, a consistent trend across the remaining samples is not evident, implying that factors other than bead size, such as salt wt % and shrinkage factor, may play more significant roles in influencing the charging rates. This theory can be further supported by the immediate charging rates following a pattern of particle size (as this will be the charge of the surface salt) but then differentiating post-initial charging period, suggesting the changes are internal effects. The initial charging rate is likely dictated by the accessibility and reactivity of the surface salt, while subsequent variations suggest a deeper complexity involving the internal structure and porosity of the beads, which in turn affects the mass transfer kinetics critical to the charging process.

Interrogation of the 150 °C static charging curves reveals an inversion between the mEG-M−S and mEG-M−M samples, challenging the assumed particle size effect. The mEG-M−M, with minimal shrinkage during synthesis, is presumed to have the highest porosity, while the mEG-M−S, experiencing the greatest shrinkage, should exhibit reduced porosity. This disparity in porosity might explain the reversal in their charging rates. The phenomenon becomes even more pronounced at the lower temperature of 120 °C, where the charging kinetics of mEG-M−S are significantly hindered, resulting in the slowest charging rate among the samples, including the largest mEG-M−L. This suggests that at reduced temperatures, mass transfer kinetics become critically affected by porosity differences between samples.

3.6.2. Dynamic charging analysis

DCA was conducted on 400 cm^3 of each composite sample in their hexahydrate state, hydrated in the same manner as the samples prepared for the SCA. Fig. 12 shows the inlet temperatures of each experiment following the 3 targeted temperature regions of 90 °C, 120 °C, and 150 °C. While the actual inlet temperatures fall short slightly of the target, the temperature profiles are consistent and only vary by a maximum of 2 °C. Even with this variation, calculations in energy utilised are based on the actual inlet temperature, and not the predicted value.

Fig. 13 shows the mass loss (A-C) and outlet temperature (D-F) profiles for each sample subjected to a flow rate of 50 l/min at each of the target temperatures. Consistent with DCA experiments conducted in previous studies [27], each sample's temperature rises to reach a wet bulb plateau before ascending to a stable final outlet temperature, which is marginally lower than the inlet temperature. This wet bulb plateau increases with increasing target charge temperature.

Although the temperature curves converge to this final equilibrium within a similar time frame, distinctive characteristics are observed during the charging process. Notably, for the smallest sample, mEG-M−XS, the ascent from the wet bulb temperature at the outlet commences latest. In contrast, the largest sample, mEG-M−L, exhibits the earliest departure from the wet bulb plateau. The intermediate-sized samples, mEG-M−S and mEG-M−M, demonstrate less obvious trends, with their temperature curves sitting between those of the smallest and largest beads.

This variability in temperature response is likely attributable to the differences in differential pressure experienced by different particle sizes within the fixed bed. Larger composites, with lower differential pressure, may enable a more consistent heat flow, whereas the smallest composite, with the highest differential pressure, may encounter resistance to heat transfer, causing the lower sections to heat more rapidly and subsequently dissipate heat upwards throughout the bed.

However, the convergence of all samples to a similar endpoint temperature within the same time frame suggests that the advantages of either heat distribution profile are marginal, with little impact on the

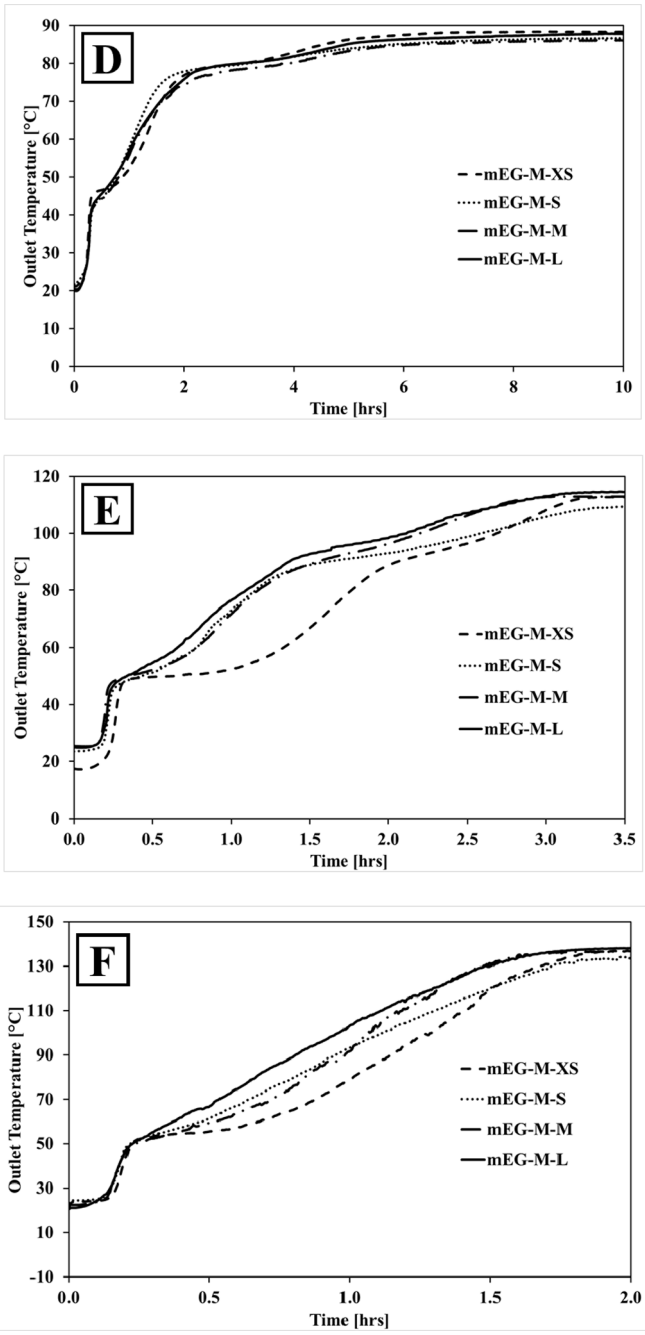

Fig. 13. (*continued*).

overall charging performance.

Across all temperature scenarios, the consistency of the mass loss curves highlights the negligible influence of particle size on the dynamic charging performance within a flow environment. This observation reinforces the previous statement that varying the heat distribution profiles does not significantly impact the in-situ charging characteristics.

In order to quantify what marginal effect particle size has on the charging performance, Fig. 14 depicts the energy required to desorb a percentage of the total mass loss. With the supplied energy calculated ($Q = mC_p\Delta T$), the energy is divided by moisture desorbed at that energy interval, offering insight into the charging efficiency comparison between composites. This is graphically represented for completing the charging process to various degrees, ranging from 50 % to 95 % charge completion.

In the charging completion range of 50–95 % for all charging temperatures there is no significant trend suggesting a superior composite size in terms of charging efficiency. At 150 °C, for charging completion between 50–80 %, a consistent pattern is observed whereby charging efficiency increases with particle size. However, at higher charging completion stages of 90 % and 95 %, the trend begins to invert with the mEG-M−XS, the smallest particle size, becoming the equally efficient as mEG-M−L. Deeper analysis of Fig. 13 shows that the time to reach 50 % completion for mEG-M−XS is 34 min whereas mEG-M−L is 39 min, again highlighting minimal difference in performance between the particle sizes. At the percentage completion of 95 %, the difference is even lesss pronounced with mEG-M−XS taking 81 min and mEG-M−L 79 min.

This inversion is more pronounced at 120 °C. At the lower charging completion stages of 50 % and 60 %, the trend again indicates that larger particle sizes are more efficient. However, by 70 % charging, efficiency

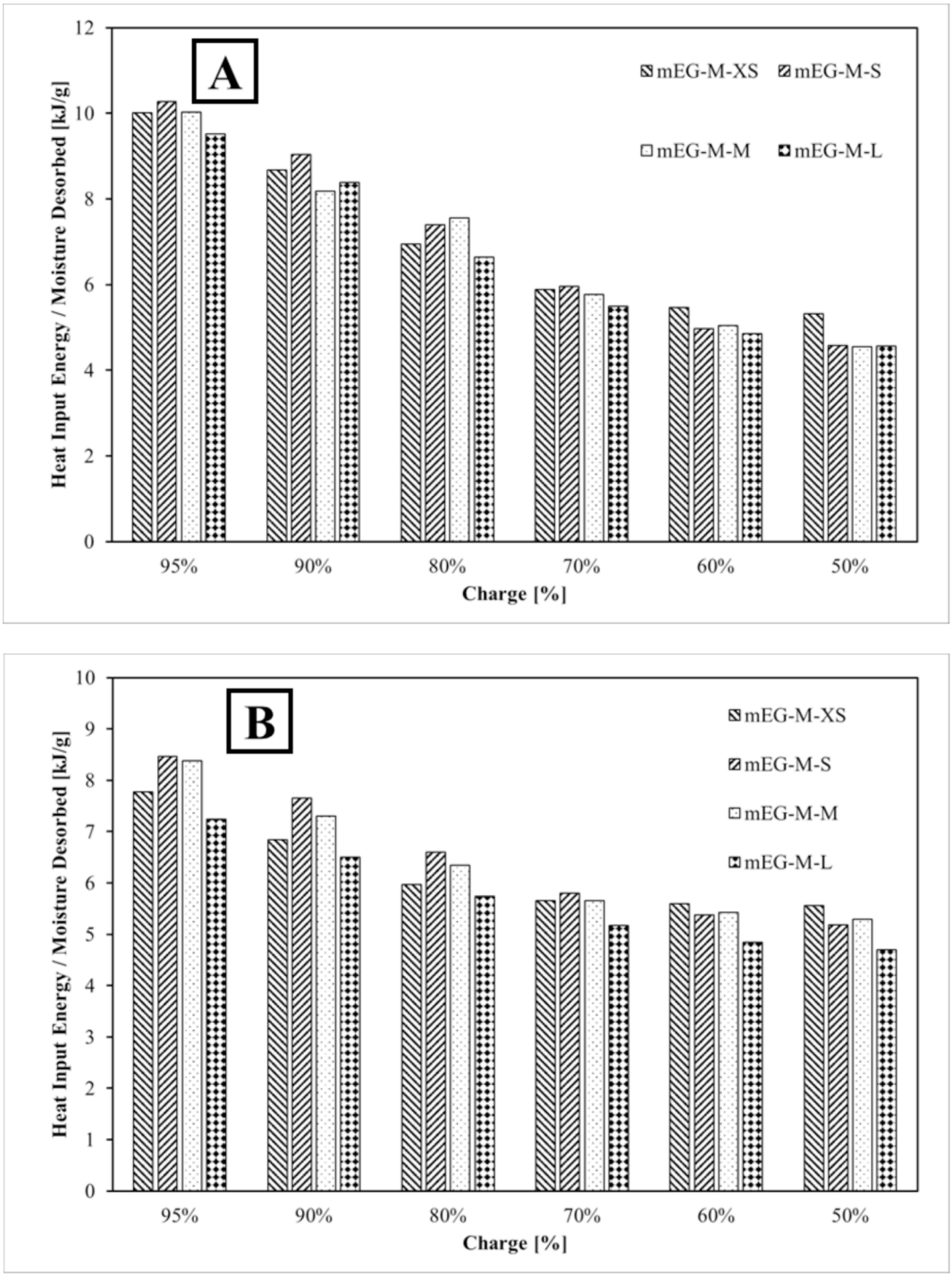

Fig. 14. Graded heat energy input required to achieve charging completion between 50–95 % for each of the four composites at flow rates of 50 l/min and flow temperatures of 90 °C (A), 120 °C (B) and 150 °C (C).

across all sizes is more consistent, beginning this reversal. By 80 % charging completion, the charging efficiency of mEG-M−XS is almost as good as mEG-M−L, an improvement on mEG-M−S and mEG-M−M. This trend is then followed through to 95 % charging completion. At 120 °C, the times to reach 50 % charge for mEG-M−XS and mEG-M−L are 54 and 49 min respectively with the trend holding at 95 % completion with mEG-M−XS requires 142 min and mEG-M−L 128 min.

Looking at the 90 °C charging, these trends are further replicated, still with a very subtle advantage of mEG-M−L and mEG-M−XS, particularly with the duration where the time to 95 % completion is 236 min compared with 253 min. As these two sizes are at either end of the size comparison for the composites, it is unlikely that the size is the only contributing factor to the patterns experienced in the charging efficiency. For all circumstances it is likely that salt wt% is also contributing to this trend, which would explain why the mEG-M−L is the most efficient. It is known from previous studies that an increase salt wt% reduces charging efficiency [27], whereby increasing the salt concentration impedes moisture removal and increases mass transfer resistance via the formation of localised crystalline salt plugs blocking the porous network. With mEG-M−L having the lowest value of 70.3 wt

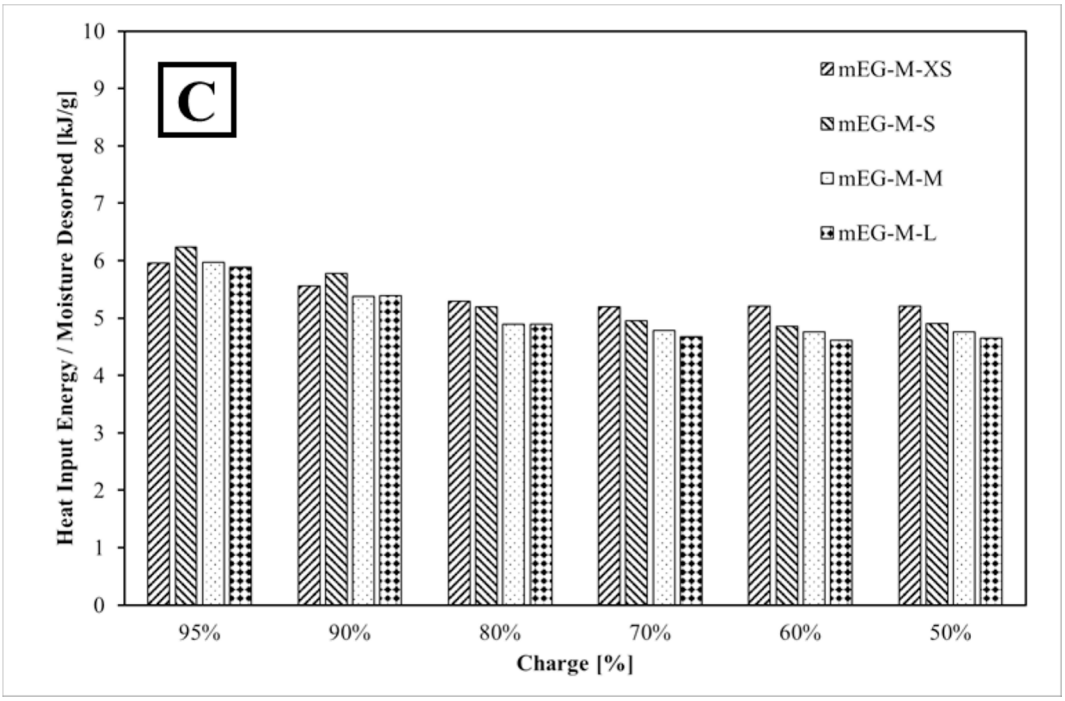

Fig. 14. (*continued*).

%, this would explain why it has improved charging efficiency, and while mEG-M−XS has the joint highest with mEG-M−M (72.9 wt%), the increase surface area improves its charging efficiency here. Porosity is also likely a contributing factor, which can be inferred by the shrinkage, and this would explain why even thought mEG-M−S has a larger surface area and smaller salt wt% than mEG-M−M, the lower shrinkage experienced by mEG-M−M improves its efficiency.

Looking at the patterns in charging efficiency between charging temperatures and charging completion percentages probes some interesting trends. At a 50 % charging completion, the charging efficiency across all three charging temperatures is consistent in the range of 5 kJ/g. However, above a 50 % charging completion, the charging efficiency differs between charging temperatures. The 150 °C charging shows the most consistent charging efficiency between 50–95 % with the 95 % charging completion on average still being below 6 kJ/g. As the charging temperature is decreased though, this difference in charging efficiency between 50 % and 95 % increases. For the 120 °C charging, the 95 % completion is around 8 kJ/g, whereas for the 90 °C charging, the 95 % completion is around 9.5 kJ/g. In terms of designing a charging apparatus for future applications such as industrial waste heat recovery, it might be beneficial to charging these materials at 90 °C for the initial 50 % expected mass loss, and then later charging at 150 °C for the remaining charging if varying temperatures flows are available.

3.7. Material economics

Economic assessment across the TCHS community is limited due to the wide range of materials investigated and limited large scale applications. Material costs at low technology readiness levels also cannot account for price competitive bulk buying and large-scale manufacturing costs. As such materials cost vary from \$3.50 kg^{-1} [40] to \$8 kg^{-1} [41], with the targets clearly being as low as possible. Bead synthesis with the assessed materials returns a cost of \$6.65 kg^{-1}.

4. Conclusions

Synthesis of composite beads within targeted diameter ranges was completed successfully, with minor variations in materials characterisation observed. Salt wt% generally decreased with increasing diameter size (72.0 % XS to 70.3 % L) whilst the salt volumetric density increased with the corresponding change. The research actually highlighted the smaller unexpected material variations that affected composite composition due to differential shrinkage factors, influencing salt wt% and bulk density. Nevertheless there were some key observations associated with the composite size.

- In terms of the differential pressure across the fixed bed the mEG-M−XS experiences significantly higher pressures than all other samples, raising concerns about potential condensation at the reactor base under certain conditions.
- XCT studies confirm that smaller diameter composites exhibit improved packing and that the void CSA distribution is inversely related to differential pressure.
- Within a dynamic sorption environment, smaller composite sizes correlate with increased total moisture uptake, while larger particles achieved a more uniform moisture distribution. During discharging reactions, smaller particle sizes were advantageous, exhibiting higher peak temperatures, prolonged peak duration, and sustained temperature elevation post a 4 h cycle.
- SCA favoured the smallest composite diameter at all three charge temperatures, likely due to the increased surface area and the reduced distance from the bead edge to the bead centre, facilitating less restricted mass transfer.
- In the dynamic charge environment, there is minimal variation in the overall charge profile, as depicted by the mass curves, despite significant variations in the temperature profiles as the charge progresses. At all three charge temperatures, there is an efficiency advantage for the larger particles up to a 50 % charge completion. However, as the charge completion approaches 95 %, the mEG-M−XS composite exhibits a comparative efficiency improvement.
- When comparing charge efficiency values across charge temperatures, there is no noticeable improvement in charge efficiency up to a 50 % charge completion by increasing the temperature from 90 °C to 150 °C. However, to achieve 95 % charge completion, the 150 °C charge maintains an efficiency close to that at 50 % charge

completion, while the efficiency at lower temperatures declines rapidly as the temperature decreases.

Within this study the charging and discharging performance of TCHS beads of a range of sizes has been categorised in both dynamic and static assessments, with initial short term cyclic performance being undertaken. The dynamic discharge cycles comprise only a single set of volumetric flow and humidity conditions, providing opportunity to explore the influence of both parameters within future studies as has been completed elsewhere [26]. Within these future studies, there is also scope to investigate reactor configuration and flow direction drawing on computational studies available within literature [35]. Further to this, the long-term cyclic performance of these composites over multiple hundreds of cycles is required to provide a true representation of the stability of these material sets both chemically and mechanically.

Declaration of competing interest

The authors declare that they have no known competing financial interests or personal relationships that could have appeared to influence the work reported in this paper.

Acknowledgements

The authors would like to thank the Materials and Manufacturing Academy and COATED CDT (COATED M2A) in Swansea University, EPSRC SUSTAIN Future Manufacturing Hub (EP/S018107/1) and the Place Based Impact Acceleration Account The SWITCH to Net Zero Buildings UKRI/EPSRC (EP/Y024060/1). X-ray micro-computed tomography was supported by the Advanced Imaging of Materials (AIM) core facility (EPSRC Grant No. EP/M028267/1), the European Social Fund (ESF) through the European Union's Convergence programme administered by the Welsh Government (80708), a Welsh Government Enhanced Competitiveness Infrastructure Grant (MA/KW/5554/19) through the European Union's Convergence programme administered by the Welsh Government.

Data availability

Data will be made available on request.

References

[1] BEIS (2022) 2020 UK Greenhouse Gas Emissions, Final Figures.
[2] CCC Mitigation Monitoring Framework - Climate Change Committee. https://www.theccc.org.uk/publication/ccc-monitoring-framework/?chapter=3-buildings#3-buildings. Accessed 20 Sep 2024.
[3] BEIS (2019) Energy Innovation Needs Assessments: Low carbon heating and cooling Sub-theme report.
[4] HM Government ; BEIS (2021) Heat and Buildings Strategy.
[5] EEA https://www.eea.europa.eu/publications/decarbonisation-heating-and-cooling.
[6] IEA https://www.iea.org/reports/renewables-2023/heat.
[7] T. Yang, W. Liu, G.J. Kramer, Q. Sun, Seasonal thermal energy storage: A techno-economic literature review, Renew. Sustain. Energy Rev. 139 (2021).
[8] A. Lyden, C.S. Brown, I. Kolo, et al., Seasonal thermal energy storage in smart energy systems: District-level applications and modelling approaches, Renew. Sustain. Energy Rev. 167 (2022).
[9] M. Gaeini, M.R. Javed, H. Ouwerkerk, et al., Realization of a 4kW thermochemical segmented reactor in household scale for seasonal heat storage, Energy Procedia 135 (2017) 105–114, https://doi.org/10.1016/j.egypro.2017.09.491.
[10] A. Krönauer, E. Lävemann, S. Brückner, A. Hauer, Mobile Sorption Heat Storage in Industrial Waste Heat Recovery, Energy Procedia 73 (2015) 272–280, https://doi.org/10.1016/j.egypro.2015.07.688.
[11] D. Mohapatra, J. Nandanavanam, Salt in matrix for thermochemical energy storage - A review, Mater Today Proc (2022), https://doi.org/10.1016/j.matpr.2022.05.453.
[12] S.P. Casey, J. Elvins, S. Riffat, A. Robinson, Salt impregnated desiccant matrices for "open" thermochemical energy storage - Selection, synthesis and characterisation of candidate materials, Energy Build 84 (2014) 412–425, https://doi.org/10.1016/j.enbuild.2014.08.028.
[13] R. Sutton, E. Jewell, J. Searle, J. Elvins, Discharge performance of blended salt in matrix materials for low enthalpy thermochemical storage, Appl Therm Eng 145 (2018) 483–493, https://doi.org/10.1016/j.applthermaleng.2018.09.052.
[14] R.J. Sutton, E. Jewell, J. Elvins, et al., Characterising the discharge cycle of CaCl2 and LiNO3 hydrated salts within a vermiculite composite scaffold for thermochemical storage, Energy Build 162 (2018) 109–120, https://doi.org/10.1016/j.enbuild.2017.11.068.
[15] S. Salviati, F. Carosio, G. Saracco, A. Fina, Hydrated Salt/Graphite/Polyelectrolyte Organic-Inorganic Hybrids for Efficient Thermochemical Storage, Nanomaterials 9 (2019) 420, https://doi.org/10.3390/nano9030420.
[16] A. Cammarata, V. Verda, A. Sciacovelli, Y. Ding, Hybrid strontium bromide-natural graphite composites for low to medium temperature thermochemical energy storage: Formulation, fabrication and performance investigation, Energy Convers Manag 166 (2018) 233–240, https://doi.org/10.1016/j.enconman.2018.04.031.
[17] Q. Miao, Y. Zhang, X. Jia, et al., MgSO4-expanded graphite composites for mass and heat transfer enhancement of thermochemical energy storage, Sol. Energy 220 (2021) 432–439, https://doi.org/10.1016/j.solener.2021.03.008.
[18] N. Gao, L. Deng, J. Li, et al., Multi-form heat storage performance of expanded graphite based CaCl2 composites for low-grade heat source, Energy Rep. 8 (2022) 12117–12125, https://doi.org/10.1016/j.egyr.2022.09.051.
[19] J. Reynolds, R. Williams, J. Elvins, et al., Development and characterisation of an alginate and expanded graphite based composite for thermochemical heat storage, J Mater Sci (2023), https://doi.org/10.1007/s10853-023-08370-1.
[20] S. Salviati, F. Carosio, F. Cantamessa, et al., Ice-templated nanocellulose porous structure enhances thermochemical storage kinetics in hydrated salt/graphite composites, Renew Energy 160 (2020) 698–706, https://doi.org/10.1016/j.renene.2020.07.036.
[21] J. Aarts, B. van Ravensteijn, H. Fischer, et al., Stabilization of salt hydrates using flexible polymeric networks, Energy 285 (2023) 129540, https://doi.org/10.1016/j.energy.2023.129540.
[22] J. Aarts, B. van Ravensteijn, H. Fischer, et al., Polymeric stabilization of salt hydrates for thermochemical energy storage, Appl Energy 341 (2023) 121068, https://doi.org/10.1016/j.apenergy.2023.121068.
[23] Y.N. Zhang, R.Z. Wang, Y.J. Zhao, et al., Development and thermochemical characterizations of vermiculite/SrBr2 composite sorbents for low-temperature heat storage, Energy 115 (2016) 120–128, https://doi.org/10.1016/j.energy.2016.08.108.
[24] A. Frazzica, V. Brancato, A. Caprì, et al., Development of "salt in porous matrix" composites based on LiCl for sorption thermal energy storage, Energy 208 (2020) 118338, https://doi.org/10.1016/j.energy.2020.118338.
[25] J. Zhu, C. Gao, F. Kong, et al., Low-priced stable SrCl2@SG composite sorbents for low-grade solar heat storage application in open sorption systems, Sol. Energy Mater. Sol. Cells 229 (2021) 111118, https://doi.org/10.1016/j.solmat.2021.111118.
[26] Walsh S, Reynolds J, Abbas B, et al (2020) Assessing the Dynamic Performance of Thermochemical Storage Materials.
[27] J. Reynolds, B. Abbas, G. Sullivan, et al., Optimisation of CaCl2 impregnated expanded graphite and alginate matrices – Targeted salt loading, Energy Convers Manag 302 (2024) 118145, https://doi.org/10.1016/j.enconman.2024.118145.
[28] H. Yang, C. Wang, L. Tong, et al., Salt Hydrate Adsorption Material-Based Thermochemical Energy Storage for Space Heating Application: A Review, Energies (basel) 16 (2023), https://doi.org/10.3390/en16062875.
[29] Zou D, Yue X, He T, et al (2022) Experimental Research on the Preparation of K2CO3/Expanded Vermiculite Composite Energy Storage Material.
[30] S. Walsh, J. Reynolds, B. Abbas, et al., Assessing the dynamic performance of thermochemical storage materials, Energies (basel) 13 (2020), https://doi.org/10.3390/en13092202.
[31] B. Fumey, R. Weber, L. Baldini, Sorption based long-term thermal energy storage – Process classification and analysis of performance limitations: A review, Renew. Sustain. Energy Rev. 111 (2019) 57–74.
[32] A. Mukherjee, R. Majumdar, S.K. Saha, et al., Assessment of open thermochemical energy storage system performance for low temperature heating applications, Appl Therm Eng 156 (2019) 453–470, https://doi.org/10.1016/j.applthermaleng.2019.04.096.
[33] L. Farcot, N. Le Pierrès, B. Michel, et al., Numerical investigations of a continuous thermochemical heat storage reactor, J Energy Storage 20 (2018) 109–119, https://doi.org/10.1016/j.est.2018.08.020.
[34] T.R.S. Gbenou, K. Wang, Study of a Thermochemical Heat Storage Reactor Filled with Polyaluminum Sulfate for Low-Temperature Application, Int J Energy Res 2024 (2024), https://doi.org/10.1155/2024/7725377.
[35] A.S. Pujari, R. Majumdar, S.K. Saha, C. Subramaniam, Annular vertical cylindrical thermochemical storage system with innovative flow arrangements for improved heat dispatch towards space heating requirements, Renew Energy 217 (2023), https://doi.org/10.1016/j.renene.2023.119168.
[36] Comet Technologies Canada Inc. https://www.theobjects.com/dragonfly.
[37] D. Zou, X. Yue, T. He, et al., Experimental Research on the Preparation of K2 CO3 /Expanded Vermiculite Composite Energy Storage Material, Materials 15 (2022), https://doi.org/10.3390/ma15103702.
[38] A. Arya, J. Martinez-Garcia, P. Schuetz, et al., Characterizing Changes in a Salt Hydrate Bed Using Micro X-Ray Computed Tomography, J Nondestr Eval 43 (2024), https://doi.org/10.1007/s10921-024-01092-7.

[39] A. Baule, H.A. Makse, Fundamental challenges in packing problems: From spherical to non-spherical particles, Soft Matter 10 (2014) 4423–4429, https://doi.org/10.1039/c3sm52783b.
[40] R.J. Clark, G. Gholamibozanjani, J. Woods, et al., Experimental screening of salt hydrates for thermochemical energy storage for building heating application, J Energy Storage 51 (2022), https://doi.org/10.1016/j.est.2022.104415.
[41] I. Bajaj, X. Peng, C.T. Maravelias, Screening and property targeting of thermochemical energy storage materials in concentrated solar power using thermodynamics-based insights and mathematical optimization, RSC Sustainability 2 (2024) 943–960, https://doi.org/10.1039/d3su00244f.